2017

A model integrating longshore and cross-shore processes for predicting long-term shoreline responses to climate change

S Vitousek

P L. Barnard

P Limber

L Erikson

B Cole

Correspondence to:
S. Vitousek,
vitousek@uic.edu

A model integrating longshore and cross-shore processes for predicting long-term shoreline response to climate change

Sean Vitousek[1] (ID), Patrick L. Barnard[2] (ID), Patrick Limber[2] (ID), Li Erikson[2] (ID), and Blake Cole[3] (ID)

[1]Civil and Materials Engineering, University of Illinois at Chicago, Chicago, Illinois, USA, [2]Pacific Coastal and Marine Science Center, United States Geological Survey, Santa Cruz, California, USA, [3]Hyperloop One, Los Angeles, California, USA

Abstract We present a shoreline change model for coastal hazard assessment and management planning. The model, CoSMoS-COAST (Coastal One-line Assimilated Simulation Tool), is a transect-based, one-line model that predicts short-term and long-term shoreline response to climate change in the 21st century. The proposed model represents a novel, modular synthesis of process-based models of coastline evolution due to longshore and cross-shore transport by waves and sea level rise. Additionally, the model uses an extended Kalman filter for data assimilation of historical shoreline positions to improve estimates of model parameters and thereby improve confidence in long-term predictions. We apply CoSMoS-COAST to simulate sandy shoreline evolution along 500 km of coastline in Southern California, which hosts complex mixtures of beach settings variably backed by dunes, bluffs, cliffs, estuaries, river mouths, and urban infrastructure, providing applicability of the model to virtually any coastal setting. Aided by data assimilation, the model is able to reproduce the observed signal of seasonal shoreline change for the hindcast period of 1995–2010, showing excellent agreement between modeled and observed beach states. The skill of the model during the hindcast period improves confidence in the model's predictive capability when applied to the forecast period (2010–2100) driven by GCM-projected wave and sea level conditions. Predictions of shoreline change with limited human intervention indicate that 31% to 67% of Southern California beaches may become completely eroded by 2100 under sea level rise scenarios of 0.93 to 2.0 m.

1. Introduction

Coastal evolution, the interaction of many geologic and hydrodynamic processes at a multitude of spatio-temporal scales, is notoriously difficult to understand let alone predict [e.g., *Pape et al.*, 2010; *Payo et al.*, 2016; *Ranasinghe*, 2016]. Nevertheless, reliable, quantitative predictions of long-term coastal evolution on decadal to centennial timescales are increasingly sought for adaptation planning in anticipation of climate change and sea level rise (SLR) [*Ranasinghe and Stive*, 2009; *Nicholls et al.*, 2016].

Nearshore hydrodynamic processes such as waves, storms, tides, currents, fluvial discharges, and sea level anomalies play significant roles in forcing short-term (e.g., seasonal to multiannual) coastal morphologic change [e.g., *Splinter et al.*, 2014; *Yates et al.*, 2009; *Hansen and Barnard*, 2010; *Coco et al.*, 2014; *Barnard et al.*, 2015]. On the other hand, long-term (e.g., decadal to centennial) processes such as natural and anthropogenic sediment supply, relative sea level changes, aeolian transport, land use, gradients in alongshore sediment transport, and climatic variations are often responsible for chronic coastal change [*Ashton and Murray*, 2006; *Warrick and Mertes*, 2009; *Sallenger et al.*, 2012]. Therefore, predicting coastal evolution on intermediate timescales (e.g., decadal to centennial) often requires accurate representations of both hydrodynamic and geologic forcing.

Many different paradigms of coastal evolution models exist to simulate behavior of certain processes and scales. Studies of coastal hazards and shoreline change due to extreme events often rely on detailed, computationally onerous, *physics-based* numerical modeling efforts [e.g., *Van Dongeren et al.*, 2009; *Barnard et al.*, 2014] to resolve the hydrodynamic forcing and morphologic response. On the other hand, simplified *process-based* or *empirical models* (detailed below) are often applied to predict chronic shoreline change. All models, however, inevitably rely upon approximations of complex, multiscale systems, and thus are subject to many sources of error [*Pape et al.*, 2010]. Nevertheless, they can provide useful tools to aid in understanding and predicting shoreline evolution.

Physics-based 2-D and 3-D models of coupled hydrodynamics, waves, sediment transport, and morphology, e.g., Delft3D [*Roelvink and Van Banning*, 1995], XBeach [*Roelvink et al.*, 2010], Mike21 [*Warren and Bach*, 1992;

Kaergaard and Fredsoe, 2013], and ROMS [*Warner et al.*, 2010], solve conservation of mass and momentum of fluid and sediment and seek to resolve nearly all of the important physical processes involved in coastal evolution. Physics-based models have become increasingly capable of simulating small-scale, short-term beach and dune erosion due to storm events on timescales of days to weeks [cf. *de Winter et al.*, 2015], and recent efforts have achieved realistic simulations on even longer timescales [*Luijendijk et al.*, 2017]. However, physics-based simulations of large-scale (e.g., 100 m to 100 km length scale) or long-term (e.g., annual to decadal timescale) shoreline change (such as beach recovery) are often prohibitively expensive in computational cost and do not necessarily provide improved skill over simplified models [*Murray*, 2007; *Ranasinghe et al.*, 2013; *French et al.*, 2016]. Therefore, a different modeling paradigm is often preferred to simulate large-scale, long-term shoreline evolution. Contrasting the physics-based approach of fully resolving the governing equations of hydrodynamic and morphologic interaction, process-based models typically account for a single dominant physical process. Process-based models, e.g., equilibrium beach profile models [*Bruun*, 1962], equilibrium shoreline models [*Miller and Dean*, 2004; *Yates et al.*, 2009, 2011; *Davidson et al.*, 2010, 2013; *Splinter et al.*, 2014], and one-line models [*Pelnard-Considere*, 1956; *Larson et al.*, 1997; *Ashton et al.*, 2001; *Ashton and Murray*, 2006], are straightforward and computationally efficient but have only been proven reliable, in most cases, on interannual timescales. Further, the accuracy of process-based models is limited in locations when unresolved, secondary processes contribute to coastal evolution. Lastly, data-driven or empirical models, constructed from observed behavior, represent another widely used paradigm to estimate long-term coastal evolution. For example, historical shoreline analyses [*Dolan et al.*, 1978; *Crowell et al.*, 1991; *Thieler and Danforth*, 1994; *Fletcher et al.*, 2003] derive rates of shoreline change from sets of orthorectified and georeferenced aerial photographs. Because empirical approaches are derived directly from observed behavior, they (implicitly) account for all relevant morphologic processes at the specific location. However, the specific processes responsible for morphologic change are not explicitly resolved. Finally, the quality of data-driven models is closely related to the quantity of data available to fit the model, and, unfortunately, shoreline data are often sparse.

As discussed above, each modeling paradigm has advantages and disadvantages. Recently, *Long and Plant* [2012] developed a data assimilation method to combine empirical and process-based shoreline models, leveraging the advantages of each approach. In this paper, we present a hybrid model with data assimilation that synthesizes and improves upon several shoreline models in the literature. The model is composed of three process-based models of sediment transport and shoreline change: (1) longshore transport and shoreline change due to waves following the one-line approach [*Pelnard-Considere*, 1956; *Larson et al.*, 1997; *Vitousek and Barnard*, 2015], (2) cross-shore transport and equilibrium shoreline change due to waves [*Yates et al.*, 2009; *Long and Plant*, 2012], and (3) cross-shore transport and equilibrium beach profile change due to SLR [*Bruun*, 1962; *Davidson-Arnott*, 2005; *Anderson et al.*, 2015].

The contributions of each of the three process-based models listed above are mutually independent and, therefore, can be summed to provide a more complete shoreline evolution model for locations of interest in a variety of geologic settings. For example, *Banno and Kuriyama* [2014] recently combined an equilibrium shoreline change model (2) and a SLR response model (3).

The proposed model is forced with sea level projections [*National Research Council*, 2012] and hindcasted (1995–2011) and forecasted (2011–2100) wave conditions derived from global-to-local nested Wave Watch III [*Tolman*, 2009] and SWAN [*Booij et al.*, 1999] wave models [*Erikson et al.*, 2015], which provide the nearshore forcing conditions needed for the process-based models. Importantly, the model uses data assimilation from historical shoreline positions to automatically calibrate the model parameters and to implicitly account for unresolved sediment transport processes, e.g., fluvial discharge, regional sediment supply, and long-term erosion. A schematic depicting the CoSMoS-COAST model, inputs, and outputs is shown in Figure 1.

Detailed discussions of the model's governing equation and its numerical method are given in sections 2 and 3, respectively. Later, in section 4, the model is applied to predict shoreline evolution on 500 km of coastline in Southern California by the end of the 21st century. Finally, section 5 presents the conclusions of this work.

2. Governing Equation

The governing equation of the CoSMoS-COAST shoreline evolution model is a partial differential equation composed of three process-based models—(1) a longshore transport one-line model, (2) a cross-shore
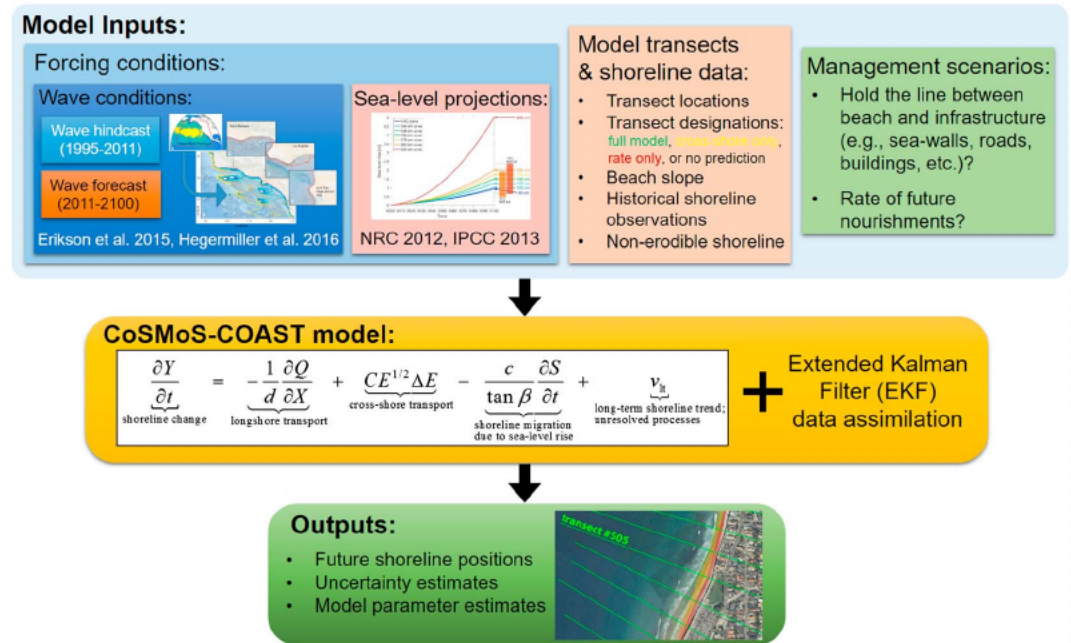
Figure 1. Overview of the CoSMoS-COAST model.

equilibrium shoreline model, (3) and a sea level driven shoreline recession model—and an assimilated long-term rate parameter due to unresolved processes. This governing equation is given by

$$
\underbrace{\frac{\partial Y}{\partial t}}_{\text{shoreline change}} = \underbrace{-\frac{1}{d}\frac{\partial Q}{\partial X}}_{\text{longshore transport}} + \underbrace{CE^{1/2}\Delta E}_{\text{cross-shore transport}} - \underbrace{\frac{c}{\tan\beta}\frac{\partial S}{\partial t}}_{\substack{\text{shoreline migration}\\\text{due to sea-level rise}}} + \underbrace{v_{lt}}_{\substack{\text{long-term shoreline trend;}\\\text{unresolved processes}}} , \tag{1}
$$

where Y represents the position of the shoreline, e.g., the mean high water (MHW) line, measured as the distance along a shore-normal transect from the onshore end of the transect (see, e.g., Figure 2), and t is time. The terms on the right-hand side (RHS), representing physical processes that force shoreline change, are discussed in the following sections.

2.1. Longshore Transport

The first term on the RHS of equation (1) is the alongshore gradient in the longshore sediment transport rate Q, where X represents the alongshore coordinate and d is the depth of closure. A generalized expression for the longshore transport rate is

$$
Q = Q_0 \sin(2\alpha), \tag{2}
$$

where Q_0 represents the magnitude of the longshore sediment transport rate derived empirically and expressed as a function of wave and sediment properties. For example, the Shore Protection Manual [*US Army Corps of Engineers*, 1984] gives $Q_0 = K \frac{\rho}{(\rho_s - \rho)\lambda} \frac{H_b^2 C_{g,b}}{16}$, where ρ is the density of water, H_b is the breaking wave height, $C_{g,b}$ is the group velocity of the wave at breaking, K is an empirically derived constant, ρ_s is the sediment density, and λ is the porosity of the sediment. The argument of equation (2), $\alpha = \alpha_{\text{wave}} - \alpha_{\text{shoreline}}$, represents the angle between the incident waves (with direction θ in Nautical convention and therefore with angle $\alpha_{\text{wave}} = 270 - \theta$ in Cartesian convention as shown in Figure 2) and the shoreline (with angle $\alpha_{\text{shoreline}}$) [*Larson et al.*, 1997]. The wave direction θ (at the offshore end of each transect) is calculated via nearshore wave models as described in section 4. The shoreline angle is given by

$$
\alpha_{\text{shoreline}} = \text{atan}\ \frac{dy}{dx} , \tag{3}
$$

where x and y represent the real world (e.g., Universal Transverse Mercator, UTM) coordinates of the
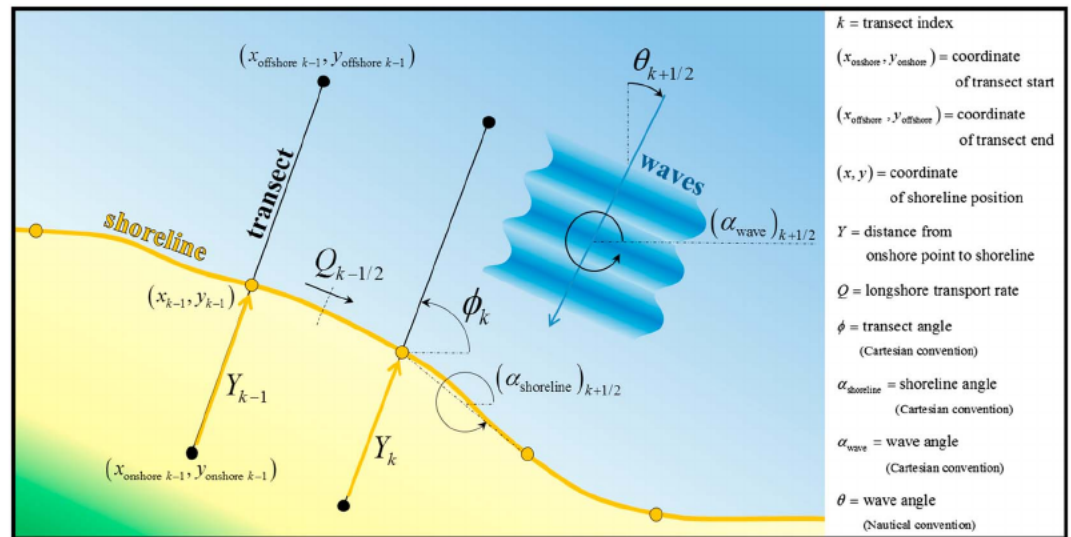
Figure 2. Schematic showing the setup of the shoreline model.

shoreline. If the alongshore and cross-shore coordinates, X and Y, are aligned with the real-world coordinates, x and y, then the upper and lower case variables are interchangeable. A schematic demonstrating the setup of the one-line model is given in Figure 2. The model does not consider high-angle wave instability and the growth of shoreline features such as spits, sand waves, and capes [e.g., *Ashton et al.*, 2001; *Falqués*, 2003; *van den Berg et al.*, 2012; *Kaergaard and Fredsoe*, 2013], which can lead to multivalued solutions to the shoreline position, Y. More details on the longshore transport component of the model are given in section 3 and Appendix A.

2.2. Cross-Shore Transport

The second term on the RHS of equation (1) is the equilibrium shoreline model of *Yates et al.* [2009], which simulates episodic beach erosion and recovery during periods of high and low wave energy, respectively. The coefficient C represents the rate of shoreline change, which we assume to remain constant during both accretion and erosion ($C = C^+ = C^-$) in order to facilitate data assimilation [*Long and Plant*, 2012]. *Yates et al.* [2011] demonstrated that replacing C^+ and C^- with C results in less than 10% degradation in model performance for California beaches. In equation (1), $E = H^2$ is the wave energy related to the wave height, H, squared. Following *Long and Plant* [2012], we do not apply a factor of 16 between the wave energy and the wave height squared, i.e., $E = \frac{1}{16}H^2$, like in *Yates et al.* [2009]. $\Delta E = E - E_{eq}$ is the disequilibrium between the instantaneous wave energy and the wave energy associated with the equilibrium shoreline position, E_{eq}. The equilibrium wave energy is given by $E_{eq} = aY_{st} + b$, where a and b are calibration parameters and Y_{st} is the short-term shoreline position described below in section 3.

2.3. Shoreline Migration Due To Sea Level Rise

The third term on the RHS of equation (1) expresses the shoreline recession resulting from passive flooding due to SLR under the assumption that the beach slope, $\tan\beta$, will remain relatively consistent through time. However, future work might consider the temporal evolution of beach slope as predicted by the parameterization of *Sunamura* [1984] and projected changes to wave breaking, wave period, and sediment size. When $\tan\beta$ is chosen as the average slope of the active beach profile extending to the depth of closure, this expression, known as the Bruun rule, approximates the shoreline recession resulting from equilibrium beach profile adjustments due to SLR, S, (or in this case the rate of SLR $\frac{dS}{dt}$) and c is a calibration coefficient. The Bruun rule is widely used [*Bruun*, 1988] and modified [*Davidson-Arnott*, 2005; *Wolinsky and Murray*, 2009; *Rosati et al.*, 2013; *Young et al.*, 2014; *Anderson et al.*, 2015], yet widely criticized [*Cooper and Pilkey*, 2004; *Ranasinghe et al.*, 2012] as an oversimplification of shoreline evolution.

If the beach slope, $\tan\beta$, is selected as the foreshore beach slope, then (in the absence of profile change) the Bruun rule simply expresses the shoreline recession due to passive flooding. This modification allows the

application of the model to rocky/cobble beaches where passive flooding is expected to occur, but the traditional Bruunian profile adjustment mechanism is not. In the application presented in section 4, we select the beach slope, $\tan\beta$, as the foreshore slope rather than the smaller average beach slope (to the depth of closure) in order to limit the influence of the Bruunian response to SLR, yet still account for migration of the shoreline due to passive flooding.

The beaches in Southern California experience some alongshore variability in foreshore beach slope, which motivates our use of a low-pass filter to smooth the beach slope in the alongshore direction for each transect. The average foreshore beach slope in Southern California, derived from LIDAR data between -2.0 m and $+2.0$ m around mean sea level at each transect, is $\tan\beta = 1/32$, suggesting (on average) 32 m of shoreline recession associated with the modified Bruunian response, $\frac{S}{\tan\beta}$, to 1.0 m of SLR. Alongshore variability can decrease or increase the local beach slope by 52% or 60%, respectively, relative to the smoothed value of the beach slope at the 95% confidence level. Therefore, the shoreline recession is sensitive to the local variability of the beach slope, which, for example, corresponds to an uncertainty (at the 95% confidence level) of -12 to $+35$ m about the mean shoreline recession of 32 m associated with 1.0 m of SLR. This method for quantifying uncertainty also applies to the unresolved temporal variability of the beach slope.

2.4. Long-Term Shoreline Trend

The fourth and final term on the RHS of equation (1) is the long-term shoreline trend that represents unresolved processes such as sources and sinks of sediment from fluvial inputs [*Inman and Jenkins*, 1999; *Willis and Griggs*, 2003; *Warrick and Mertes*, 2009], nourishments [*Flick*, 1993], cliff failure [*Young et al.*, 2011; *Limber and Murray*, 2011], aeolian transport [*Bauer et al.*, 2009], sand mining [*Thornton et al.*, 2006], and transport from offshore [*Schwab et al.*, 2013]. In equation (1), if the long-term trend, v_{lt}, is a constant, then the shoreline migration is linear in time. Historical shoreline analyses using aerial photos often use linear regressions to fit observed shoreline data and determine long-term annual erosion rates [see, e.g., USGS National Assessment of Shoreline Change; *Hapke et al.*, 2006]. The data assimilation method assumes that v_{lt} is constant, starting from an initial value of $v_{lt} = 0$. However, when a data assimilation step takes place, the magnitude of v_{lt} changes and thus the unresolved, long-term shoreline change is time dependent. During the model forecast period, no observations are available to assimilate. Thus, during the forecast period v_{lt} is constant, and therefore, the unresolved, long-term shoreline change associated with this term is linear in time. Thus, this long-term component is subject to error when chronic, unresolved processes result in a nonlinear response. The magnitude of this error, although difficult to assess a priori, may be parameterized via process noise in the Kalman filter as described in section 3 and Appendix B. In the application presented in section 4, v_{lt} represents (on average) approximately 10% of the variability of the shoreline change over long periods (~50 years and longer). However, regions dominated by nourishments or other long-term effects may have locally high values of v_{lt}.

3. Numerical Model

3.1. Spatial Discretization

In the proposed model, the coastline is discretized into a series of shore-normal transects that are arbitrarily spaced in the alongshore direction. For each transect, the shoreline position at a given time step is measured by the distance, Y, from the onshore end of the transect. The model computes the evolution of Y for each transect. Accordingly, the shoreline evolves as if "on rails" represented by each transect. A schematic of the model domain is shown in Figure 2. Although there are long-term coastal evolution models that are grid based (e.g., the Coastal Evolution Model (CEM) of *Ashton and Murray* [2006]) and vector based [*Hurst et al.*, 2015], the current model is chosen to be transect based to cover long, irregular coastlines and facilitate the composition of the 1-D, process-based models (described above) with data assimilation. The drawback to the transect-based discretization is that, unlike CEM and many physics-based numerical models, the numerical method presented here does not have a conservative formulation for sediment volume. However, this characteristic does not severely denigrate the model quality, because of our inherent inability to resolve all processes resulting in shoreline evolution. Furthermore, the data assimilation method precludes the model from conserving sediment volume because the shoreline position and long-term shoreline change rate are intermittently adjusted to best fit the observations.

3.2. Temporal Discretization

The model uses explicit Euler time stepping [see, e.g., *Moin*, 2010] for the cross-shore transport terms due to waves, sea level, and long-term effects. Fortunately, these terms do not exhibit numerical instability. The longshore-transport term, on the other hand, is susceptible to numerical instability based on the Courant number condition $\Delta t < \frac{\Delta X^2 d}{4 Q_0}$ [*Ashton and Murray*, 2006; *Vitousek and Barnard*, 2015]. Accordingly, the model uses the option of explicit Euler time stepping or the semi-implicit time stepping of *Vitousek and Barnard* [2015] (see Appendix A for details). The transect spacing, ΔX, is the most important consideration in selecting the preferred time stepping method. In general, explicit Euler time stepping suffices for transects spaced approximately 100 m or greater.

3.3. Model Equations

To facilitate model construction and data assimilation, equation (1) is split into short- (seasonal cross-shore transport) and long-term (longshore transport, SLR effects, and other) components of shoreline change, Y_{st} and Y_{lt}, respectively, where $Y = Y_{st} + Y_{lt}$ following *Long and Plant* [2012]. This splitting procedure applies the correct wave energy disequilibrium, $E_{eq} = a Y_{st} + b$, associated with the short-term shoreline position, Y_{st}. Wrongly setting $E_{eq} = a Y + b$ results in spurious disequilibrium between the wave energy and the new long-term shoreline position, driving nonphysical shoreline change (e.g., spurious short-term accretion on a chronically eroding shoreline and vice versa).

The split model equations become

$$\frac{(Y_{st})_k^{n+1} - (Y_{st})_k^n}{\Delta t} = C_k \left(E_k^n\right)^{1/2} \left(E_k^n - a_k (Y_{st})_k^n - b_k\right) \tag{4}$$

$$\frac{(Y_{lt})_k^{n+1} - (Y_{lt})_k^n}{\Delta t} = -\frac{K_k}{d_k} \frac{Q_{k+1/2}^{n+\theta} - Q_{k-1/2}^{n+\theta}}{\Delta X_k} - \frac{c_k}{\tan\beta_k} \left(\frac{\partial S}{\partial t}\right)_k^n + (v_{lt})_k, \tag{5}$$

where superscripts n represent the time step index, Δt is the time step, k represents the transect index, and ΔX_k is the distance between adjacent transects (given in Appendix A). Note that the longshore-transport parameter, K_k, is taken outside of the longshore transport rate, Q, in equation (5), in order to facilitate data assimilation of the parameter, as discussed below. All of the model parameters and variables in equations (4) and (5) are defined at each transect (with index k) except the longshore transport rate, Q, which is located between adjacent transects (with indices $k \pm 1/2$). Details of the longshore transport component of the model and the implicitness parameter θ ($0 \leq \theta \leq 1$) are given in Appendix A.

3.4. Data Assimilation

Data assimilation automatically adjusts the model parameters during runtime to best fit any available observed shoreline data at the concurrent time step. Equations (4) and (5) use the extended Kalman filter data assimilation method of *Long and Plant* [2012]. The state vector representing the model solution and parameters is given by $\psi = \begin{bmatrix} Y_{lt} & v_{lt} & Y_{st} & C & a & b & c & K \end{bmatrix}^T$. Following equations (4) and (5), the evolution of the state vector is given by

$$\frac{\partial \psi_k}{\partial t} = \frac{\Psi_k^{n+1} - \Psi_k^n}{\Delta t} = \begin{bmatrix} -\frac{K_k}{d_k} \frac{Q_{k+1/2}^{n+\theta} - Q_{k-1/2}^{n+\theta}}{\Delta X_k} - \frac{c_k}{\tan\beta_k} \left(\frac{\partial S}{\partial t}\right)_k^n + (v_{lt})_k \\ 0 \\ C_k \left(E_k^n\right)^{1/2} \left(E_k^n - a_k (Y_{st})_k^n - b_k\right) \\ 0 \\ 0 \\ 0 \\ 0 \\ 0 \end{bmatrix} = \mathbf{f}_k^n. \tag{6}$$

The evolution equation of the state vector, equation (6), has zero right-hand side terms, $\frac{\partial \psi_k}{\partial t} = 0$, for the evolution of the six model parameters, $\psi_k = (v_{lt})_k, C_k, a_k, b_k, c_k, K_k$, that represent spatially variable, yet temporally constant coefficients, which are updated at each data assimilation step. Note that in equation (6), terms with superscript n (e.g., $Q_{k\pm1/2}^{n+\theta}$, E_k^n, and $\frac{\partial S}{\partial t}_k^n$, which represent the wave and sea level forcing conditions)

are variable in time. On the other hand, terms without superscript n are assumed to be constant with time in the absence of data assimilation (e.g., $(v_{lt})_k, C_k, a_k, b_k, c_k, K_k$ and the unassimilated parameters d_k and $\tan\beta_k$), although in reality all of these parameters can exhibit variability in time, inevitably resulting in model error. The data assimilation method in equation (6) takes place independently for each transect k, meaning that the model of a given transect is only aware of the shoreline data falling on that individual transect at that instance in time. The numerical procedure of the data assimilation method is detailed as follows:

(1) Compute the evolution of the state vector, $\psi_k^* = \psi_k^n + \Delta t \mathbf{f}_k^n$, using the forward model, equation (6). Without data to assimilate, $\psi_k^{n+1} = \psi_k^*$.
(2) Compute the Jacobian, $\mathbf{J}_{ij} = \frac{\partial \mathbf{F}_i}{\partial \psi_j}$ for each transect, where $\mathbf{F}(\psi_k^n) = \psi_k^n + \Delta t \mathbf{f}_k^n$.
(3) Update the error covariance matrix, $\mathbf{P} = \mathbf{J}\mathbf{P}\mathbf{J}^T + \mathbf{Q}$, where $\mathbf{Q}$ is the process noise.
(4) Compute the Kalman Gain, $\mathbf{K} = \mathbf{P}\mathbf{H}^T(\mathbf{H}\mathbf{P}\mathbf{H}^T + \mathbf{R})^{-1}$, where $\mathbf{R}$ is the measurement error and $\mathbf{H} = \begin{bmatrix} 1 & 0 & 1 & 0 & 0 & 0 & 0 & 0 \end{bmatrix}^T$ is the vector that relates the state vector to the observations.
(5) Compute the data-assimilation step, $\psi_k^{n+1} = \psi_k^* + \mathbf{K}\left((Y_{obs})_k^{n+1} - \mathbf{H}\psi_k^*\right)$, where $(Y_{obs})_k^{n+1}$ is the observed shoreline position at transect, k, and between time steps n and $n+1$.
(6) Compute the final error covariance matrix, $\mathbf{P} = (\mathbf{I} - \mathbf{K}\mathbf{H})\mathbf{P}$, to be used in the following time step.

If no concurrent data is available to assimilate at a given time step, then steps 4–6 are skipped. Note that steps 2 and 3 must take place every time step (even without data to assimilate) in order to allow data assimilation at future time steps.

Under the assumption of temporal constancy of model parameters, it is possible to make long-term predictions of shoreline position (given the right forcing conditions), and the Kalman filter is simply used as a large-scale calibration tool. Knowledge of good initial parameters and the lack of unresolved processes eliminates the need for the Kalman filter. Although the proposed model assumes temporal constancy of its parameters, long-term geologic processes may invalidate this assumption in certain coastal settings and require modification to current model. For example, equation (6) could be reformulated with a user-specified, time-varying formulation of the dynamic effects, $\frac{\partial \psi}{\partial t} = f(t) \neq 0$. However, this approach will likely require longer data records to assimilate the parameters involved in the dynamic effects, i.e., $f(t)$, which, for example, may represent long-term changes in sediment composition or beach slope.
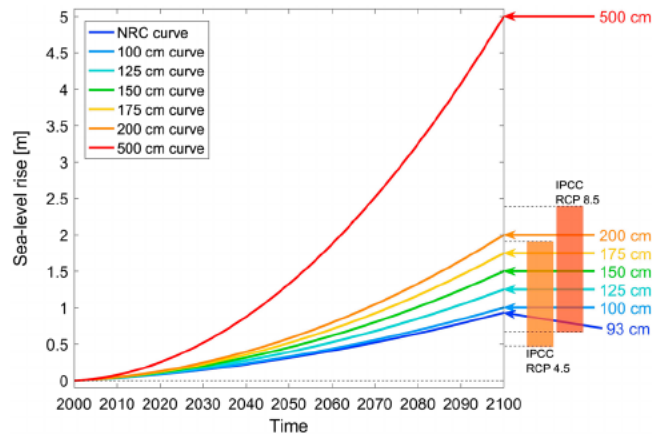
Based on previous work [*Yates et al.*, 2009; *Long and Plant*, 2012; *Doria et al.*, 2016], we expect that the wave-driven, cross-shore transport parameters C, a, b are nearly constant in time. Based on this assumption, changes in shoreline position resulting from (well-resolved) changes in wave climate [*Erikson et al.*, 2015] would be captured with the model. We also anticipate that c and K are roughly constant in time; however, long-term changes in beach profile and sediment composition may alter these coefficients in unpredictable ways. The most uncertain and temporally variable parameter is v_{lt}. Lacking better options, the proposed model treats v_{lt} as a constant like in *Long and Plant* [2012] and in most historical erosion rate analyses (e.g., the USGS National Assessment of Shoreline Change [*Hapke et al.*, 2006]). However, nonlinear changes in natural or anthropogenic sediment supply and changes taking place outside of the hindcast period will not be resolved in the current model.

Finally, we note that many of the model parameters have requisite signs. Parameters C and a are negative and b, c, and K are positive. Instability results when the data assimilation method inadvertently changes a parameter's expected sign. To prevent this instability, the numerical method, equation (6), is modified to ensure that the parameters retain their requisite signs throughout the data assimilation step. Details of the sign-preserving data assimilation method are presented in Appendix B.

4. Application

The CoSMoS-COAST model was developed as the shoreline change component of the Coastal Storm Modeling System (CoSMoS) framework [*Barnard et al.*, 2014], focusing on the U.S. West Coast. The initial framework focused on developing predictions of coastal flooding due to waves and sea level rise on present-day shoreline configurations. However, chronic erosion, driven by accelerating rates of sea level rise, might exacerbate future coastal flooding, and applying present-day beach profiles to flood prediction models might underestimate future hazard vulnerability. Thus, CoSMoS-COAST was developed to understand the effects of shoreline change and its impact on future flooding due to waves and sea level rise.

Figure 3. Scenarios of SLR used in the CoSMoS-COAST application to Southern California.

4.1. Sea Level Rise Forcing

Sea level versus time is modeled as a quadratic function. The three unknown coefficients of the quadratic curve are obtained via three equations.

(1) The mean sea level in 2000 is assumed to be at zero elevation.

(2) The rate of SLR in 2000 is assumed to be at 3 mm/yr, which is consistent with values observed via satellites and local tide gages.

(3) Future sea level elevation at 2100 is assumed to be 0.93 [*National Research Council*, 2012], 1.0, 1.25, 1.5, 1.75, 2.0, and 5.0 m based on the scenarios considered (see Figure 3).

The chosen sea level scenarios closely reflect the 2100 predictions given in the Intergovernmental Panel on Climate Change 2013 (IPCC 2013) report (Figure 13.9 in *Church et al.* [2013]) as shown in Figure 3. We note that sea level only affects the equilibrium profile changes via the third term on the RHS of equation (1).

4.2. Wave Forcing

Climate change drives potential changes to wave climate [*Hemer et al.*, 2013; *Erikson et al.*, 2015; *Shope et al.*, 2016], which must be accounted for when predicting long-term coastal evolution. CoSMoS-COAST is driven with hindcast (1995 to 2011) and projected time series (2011 to 2100) of daily maximum wave heights and corresponding wave periods and directions from *Erikson et al.* [2015] and *Hegermiller et al.* [2016], who used a series of global-to-local nested wave models (i.e., WaveWatch III (WW3) and SWAN), shown in Figure 4. Hindcast waves are computed with NOAA WW3 Climate Forecast System Reanalysis and Reforecast hindcast deep-water waves applied at the open boundaries of a high-resolution SWAN grid and Scripps Institution of Oceanography reanalysis winds across the entire domain so that both swell and local sea generation are accounted for in the simulations. In order to improve efficiency, projected wave conditions at each model transect are generated via lookup tables constructed from results of the high-resolution hindcast [*Hegermiller et al.*, 2016]. Deep-water wave forcing, derived from global and regional scale WW3 simulations [*Erikson et al.*, 2015], and projected wind fields from global climate models are used as inputs to the lookup table. The wave climate projections employed in this application uses the GFDL-ESM2M climate model [*Delworth et al.*, 2006] and representative concentration pathway (RCP) 4.5 emissions scenario [*Stocker*, 2014]. Accurate predictions of nearshore wave conditions are needed because the formulations in equation (1) are highly sensitive to wave conditions. In particular, variations in wave angle and wave energy can significantly affect the calculation of longshore transport (via equation (2)) and equilibrium shoreline response, respectively. In the current application, the shoreline model is forced with a single projected time series of wave conditions [from *Hegermiller et al.*, 2016]. However, this wave forcing scenario represents only one instance of the stochastic system representing the future wave climate. Use of an ensemble wave forcing approach would likely improve the range of potential shoreline positions and estimates of uncertainty but at the cost of increased computational effort (by a factor representing the number of ensemble wave scenarios). Adoption of an ensemble approach would likely favor computationally efficient lookup table methods (used here) or statistical downscaling methods [*Antolínez et al.*, 2015; *Rueda et al.*, 2017] over dynamical downscaling (nested models).
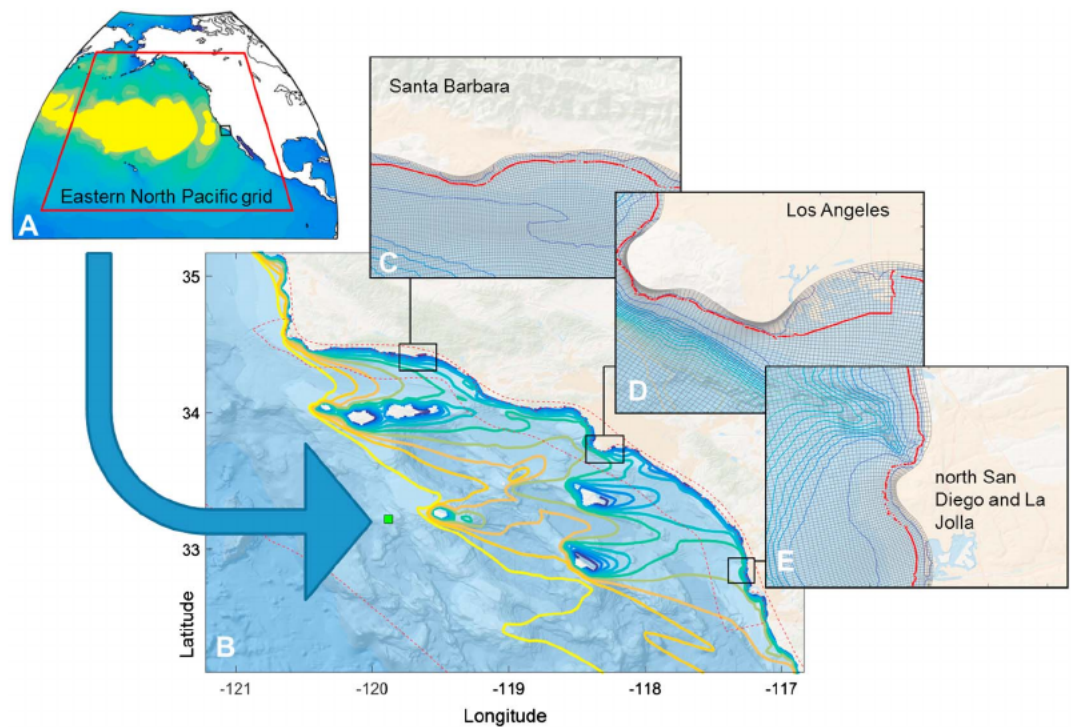
4.3. Transects

The ~500 km domain of the Southern California coast is discretized into 4802 transects spaced approximately 100 m apart (see Figure 5). The offshore ends of each transect coincide with the Model Output Points transects [*Coastal Data Information Program*, 2016] used in previous CoSMoS modeling efforts [*Barnard et al.*, 2014]. Each transect was manually given a designation of "full model," "cross-shore only," "rate only," or "no prediction" based on geologic characteristics. Based on the transect designation, the shoreline model retains or neglects certain physical processes and the corresponding terms in the governing equation

Figure 4. Wave grids from *Erikson et al*. [2015] and *Hegermiller et al*. [2016] used in the CoSMoS-COAST application to Southern California. (a) The boundaries of the Eastern North Pacific WaveWatch3 grid and typical extratropical storm tracks producing large wave heights in yellow. (b) The boundaries of the West Coast and Southern California SWAN grids (red dashed lines) as well as bathymetry (blue base map) and contours of wave height illustrating wave shadowing by offshore islands (yellow, orange, and blue contours). (c–e) The wave grids, bathymetry, and offshore ends of each transect (red dots) in the Santa Barbra, Los Angeles, and San Diego regions, respectively.

(equation (1)). As the name implies, transects designated as "full model" evolve the shoreline using the full governing equation (equation (1)). "Full model" transects are selected for long, sandy beaches, and all model components are included. Small (<1 km), sandy pocket beaches (with limited longshore transport and localized hydrodynamic effects [e.g., *Daly et al*., 2011; *Gallop et al*., 2011; *Castelle and Coco*, 2013; *van de Lageweg et al*., 2013; *Ratliff and Murray*, 2014; *Harley et al*., 2015]) are designated as "cross-shore only" by setting $K = 0$. Cobble beaches and heterogeneous sandy/rocky beaches invalidate the process-based models used here and, therefore, are designated as "rate only" transects by neglecting longshore and cross-shore transport due to waves, i.e., setting $K = 0$ and $C = 0$. These transects evolve the shoreline using a linear change rate (obtained via data assimilation) plus a recession rate due to excess passive flooding above the current rate of SLR [*Anderson et al*., 2015]. Finally, "no prediction" transects represent harbors, armored and rocky shorelines, and sea cliffs (without fronting beaches) where no model calculations are performed. In the current application in Southern California (Figure 5), 40% of the transects are "full model," 29% are "cross-shore only," 15% are "rate only," and 16% are "no prediction."

4.4. Shoreline Data

Assimilation of historical shoreline data is a critical component of the model. Each shoreline observation provides an opportunity to nudge the model parameters closer to their "true" state. Without data to assimilate, model skill depends on the accuracy of the estimated model parameters. For the shoreline forecast period (2010–2100), no observations are available and thus no data assimilation can be performed. Therefore, the model hindcast period must assimilate enough shoreline data to allow sufficient convergence of the model parameters before the start of the forecasting period (see Appendix C for details on convergence of the model parameters).

Historical shoreline data are often spatially and temporally sparse. The current application combines the two most recent mean high water (MHW) shorelines (years 1997 and 2009) of the USGS National Assessment of

Figure 5. CoSMoS transects for Southern California. (Basemaps from Google Earth).

Shoreline Change [*Hapke et al.*, 2006], 20 MHW shorelines derived from coastal LIDAR surveys (2003–2009; many of which only cover the southern half of the study area, i.e., south of Long Beach harbor) and 20 MHW shorelines derived from biannual (2005–2015) GPS surveys by the USGS in Santa Barbra [*Barnard et al.*, 2009]. An example of the shoreline data used in this application is shown in Figure 6 for La Jolla Shores. Each intersection of a shoreline vector and a model transect provides one data point in time for data assimilation (see Figure 6b). This data set provides a number between a minimum of 2 and a maximum of 27 shorelines to assimilate at a given transect. The average number of shorelines available on each transect is 12. Although the current model uses a significantly larger number of shorelines than studies of comparable scale (e.g., the USGS National Assessment of Shoreline Change used only five shorelines in California), it is likely that even more data are required to develop a truly predictive model of long-term shoreline change. This suggests that continued shoreline monitoring efforts, e.g., seasonal coastal LIDAR surveys, are critical assets to understand and predict shoreline change.

4.5. Coastal Management Scenarios

In this application, we explore the combination of seven sea level projections (see Figure 3) and four management scenarios. The four management scenarios result from two independent, binary scenarios, namely, "hold the line" and "continued nourishment." The "hold the line" scenario represents the management decision to prevent or allow the shoreline from receding past existing infrastructure (e.g., by permitting or prohibiting shoreline armoring, respectively). If the line is held, then the modeled shoreline is constrained from eroding past a 180,000-point polyline manually digitized from aerial photos that represent the division of beach and urban infrastructure or the division of the subaerial beach and coastal cliff. We note that the "hold the line" scenario is implemented in the model by setting $Y^{n+1} = \max(Y^{n+1}, Y_{\text{non-erodible}})$ without constraining the model parameters. If the line is not held, then the shoreline is allowed to erode into existing infrastructure and coastal cliffs (i.e., $Y < Y_{\text{non-erodible}}$ is permitted).

In this initial model application, we assume that the cliff does not erode landward with the beach, and the non-erodible shoreline stays fixed through time. Thus, the dynamics between cliff erosion and beach change, where the eroding cliff provides sediment to the beach and the beach width controls cliff
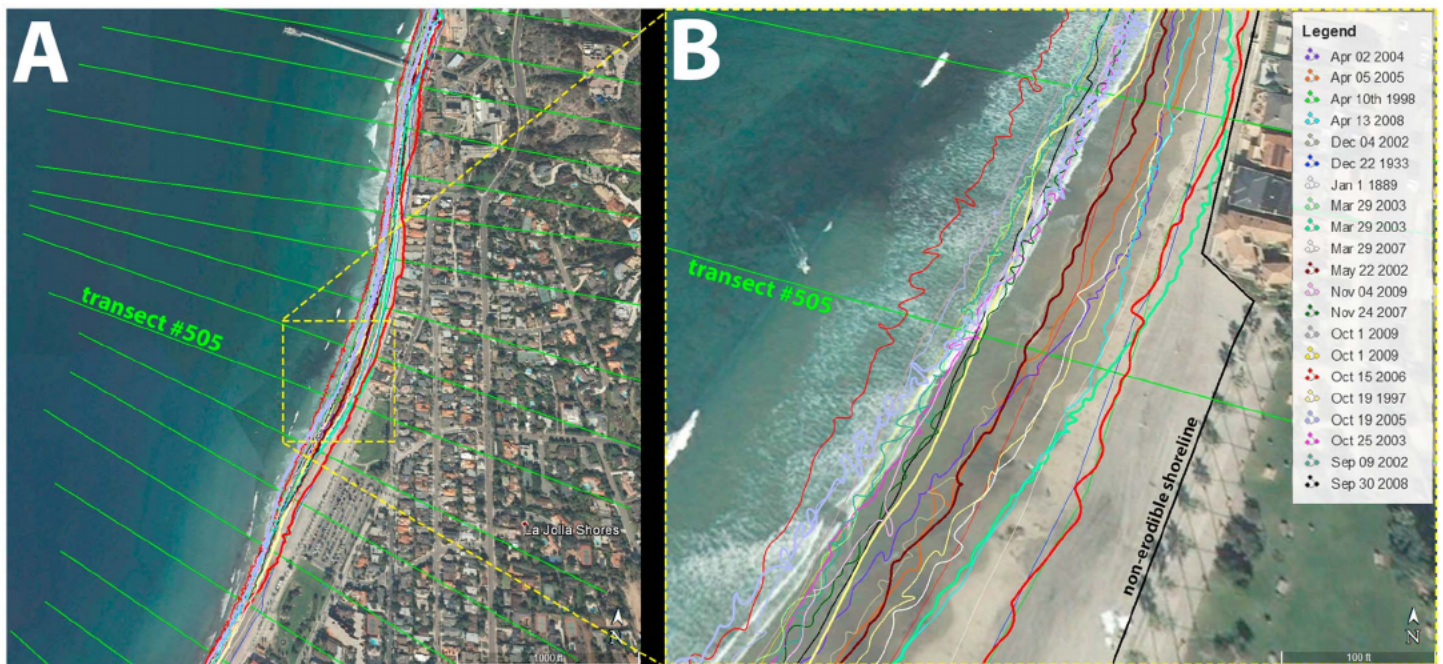
Figure 6. An example of the shoreline data, pictured above for La Jolla Shores, used in the CoSMoS-COAST model. (Basemaps from Google Earth).

erosion [e.g., *Limber and Murray*, 2011; *Limber et al.*, 2014], do not apply here. In future model applications, the CoSMoS-COAST model and a cliff retreat model [*Limber et al.*, 2015] will be coupled together.

The "continued nourishment" scenario represents the management decision to continue or cease the long-term, business-as-usual beach nourishment rate determined from recent historical data (1995–2010). The USGS National Assessment of Shoreline Change [*Hapke et al.*, 2006] derived long-term erosion rates from historical aerial photos in Southern California and found that a majority of the beaches are accreting. However, anthropogenic beach nourishments dominate these rates of accretion and mask the natural signal of shoreline change [*Flick*, 1993; *Hapke et al.*, 2006]. Thus, we conduct two scenarios assuming that recent historical accretion trends either continue until 2100 or cease after 2010 (when data to assimilate become unavailable). In the model, the "continued nourishment" scenario is implemented by either allowing the data-assimilated value of v_{lt} to remain unchanged during the forecast period (2010–2100). On the other hand, the "no continued nourishment" scenario forces $v_{lt} = 0$ following the final data assimilation step for each accreting transect where $v_{lt} > 0$. The seven sea level scenarios and four management scenarios combine to give a total of 28 different models run as part of this effort.

4.6. Results

As a preliminary analysis, we estimate the historical, long-term rate of shoreline change using a linear regression of time versus observed shoreline position, obtained from the intersection of the shoreline vectors at each transect (see, e.g., Figure 6). This effort is intended to update and improve upon previous estimates of the Southern California historical shoreline change rate [*Hapke et al.*, 2006] through the inclusion of additional shoreline data. The long-term shoreline change rate (in m/yr) versus transect number is shown in Figure 7. Note that the colored bands in Figure 7 identify the littoral cells identified by *Flick* [1993] associated with each transect. The results here reiterate the findings of *Hapke et al.* [2006]: A majority of the beaches in Southern California are accreting (72% of the transects). The regression rates (in Figure 7) alone do not identify the causal mechanisms of shoreline accretion. However, the shoreline change rates in Figure 7 do suggest a strong anthropogenic influence (as was established in *Flick* [1993] and *Hapke et al.* [2006]) based on the observation that the largest rates of shoreline change occur near harbors and beaches receiving significant nourishments.

It is possible to extrapolate a prediction of future shoreline position from long-term, historical shoreline change rates. However, because the rates are predominantly accretionary, a naïve extrapolation of
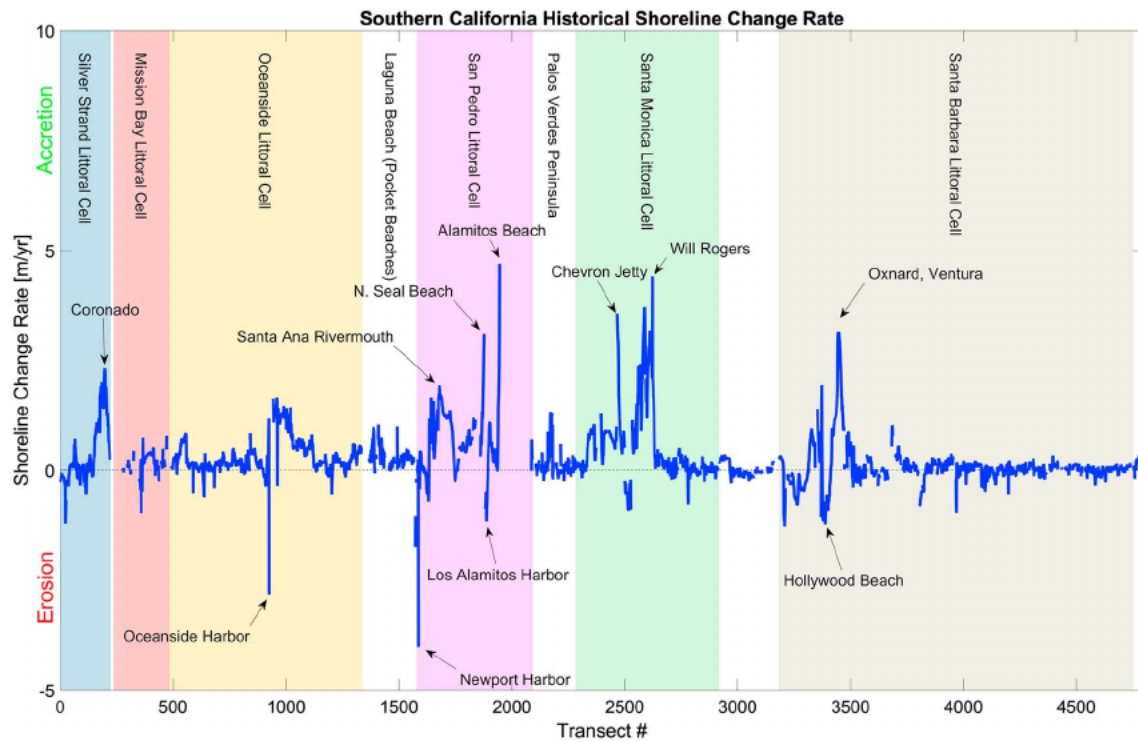
Figure 7. Long-term shoreline change rates for Southern California. Colored bands identify the littoral cells delineated in *Flick* [1993].

shoreline position can significantly overestimate future beach width and thus underestimate future coastal hazard potential. Furthermore, predictions based on linear extrapolation methods neglect dynamical processes such as seasonal beach profile changes and accelerated sea level rise. Thus, the proposed dynamical model is applied to improve long-term predictions of shoreline change while accounting for the relevant physical processes and management practices.

The proposed dynamical model, equations (B8) and (B9) in the Appendix B following from equations (4) and (5), is applied to Southern California. The model starts on 1 January 1995 and is run until 1 January 2100 with a time step of 1 day. Data assimilation takes place at each time step when a concurrent shoreline observation is available for a given transect. At each data assimilation step, the model parameters are adjusted to best fit the dynamical model with the observed shoreline positions. When no more shoreline data is available to assimilate (date of last observed shoreline—typically in Fall 2010), the forward model provides a forecasting tool based on the converged values of the model parameters at each transect.

The model-predicted final shoreline position in 2100, Y, relative to the initial shoreline position in 1995, Y_0, and spatial variability (with transect number) of the final values of the assimilated model parameters are shown in Figure 8. The uncertainty values, estimated directly from the Kalman filter, arise from the process noise estimates **P** and **Q** as discussed in Appendix B. Note that Figure 8 applies the same colored bands in Figure 7 to indicate the littoral cells identified by *Flick* [1993] associated with each transect. The initial values (blue lines in Figure 8) of a few model parameters are assumed constant for all transects: $C = 0.5$, $a = 0.1$, and $v_{lt} = 0$, which represent nominal values based on previous work [e.g., *Yates et al.*, 2009]. The initial values of parameter b are set to the average significant wave height for each transect, and the initial values of parameter K are estimated from variations in sediment type and grain size according to Table 1. Also, note that some model parameters are set to zero according to their transect designation (i.e., "cross-shore only," "rate only," or "no prediction") when specific physical processes are neglected.

Figure 8 demonstrates the considerable alongshore variability in the final values of the model parameters, especially for the equilibrium shoreline model parameters C, a, and b. We compare the data-assimilated parameters C and a to the range of values reported in *Yates et al.* [2009] and *Doria et al.* [2016] for Camp Pendleton, Cardiff/Solana Beach, Torrey Pines, and Imperial Beach (green bands in Figures 8b and 8c). The
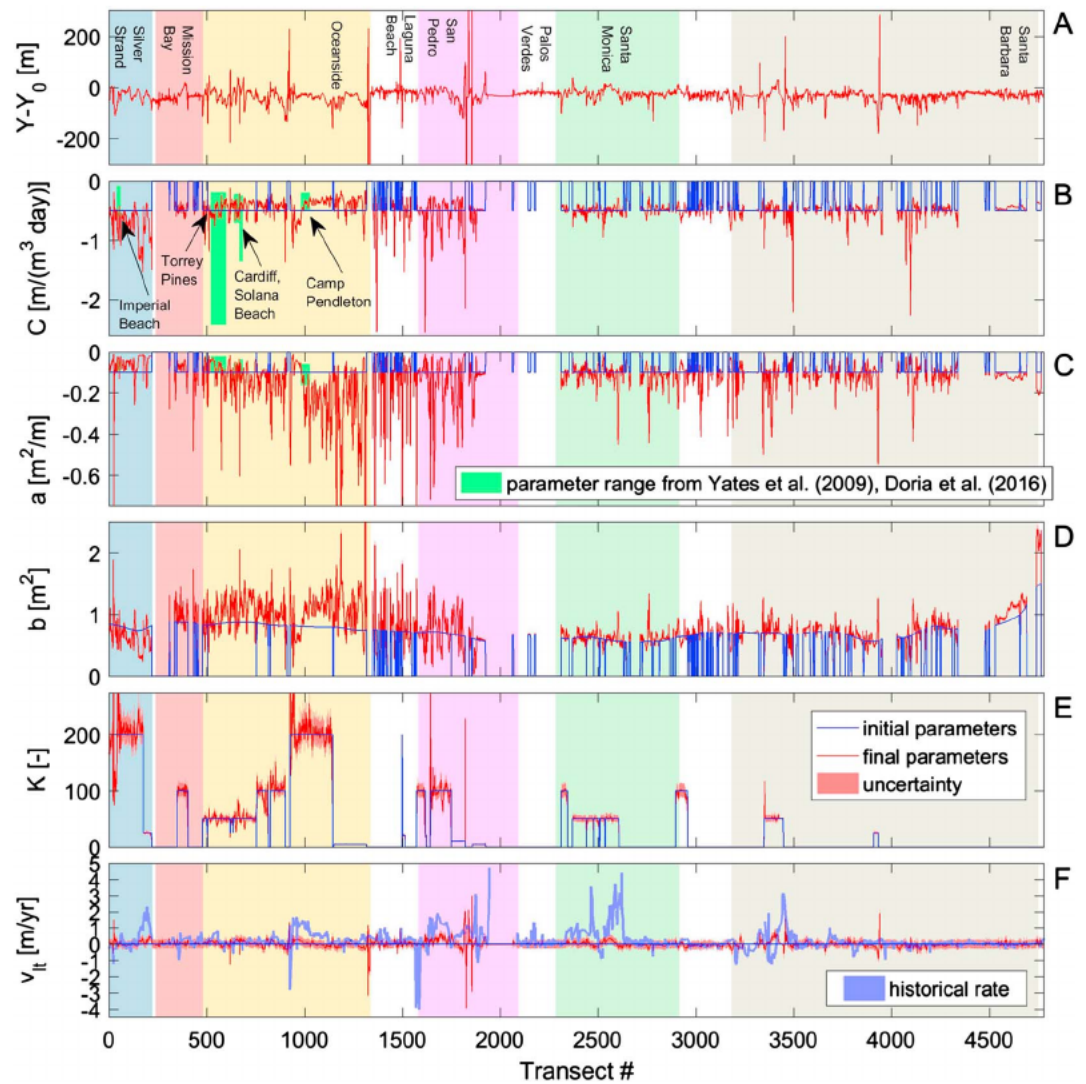
Figure 8. (a–f) The final shoreline position and assimilated coefficients of the CoSMoS-COAST model applied to Southern California. The blue line represents the initial values of the shoreline model coefficients (note that $K \neq 0$ for all "full model transects"; $C = a = b = K = 0$ for all "rate only" transects; and $v_{lt} = 0$ for all "no prediction" transects), the red lines represent the final assimilated values of the coefficients, and the pink bands represent uncertainty. Colored bands identify littoral cells delineated in *Flick* [1993]. The green bands in Figures 8b and 8c represent the range of parameters C and a, respectively, reported in *Yates et al.* [2009] and *Doria et al.* [2016].

excellent agreement between parameters C and a derived in CoSMoS-COAST and *Yates et al.* [2009]/*Doria et al.* [2016] demonstrates the strong performance, the proposed data assimilation method, and its applicability to large spatial scales. Figure 8f shows the assimilated long-term shoreline change rate, v_{lt}, compared to the historical shoreline change rate (Figure 7). As expected, the assimilated and historical rates for each transect demonstrate a vague agreement, with the assimilated rates having a smaller

Table 1. The Longshore Transport Rate Coefficient, K, Used in the Current Application in Southern California Based on the Sediment Type and Grain Size

Sediment Type	Grain Size	Grain Diameter (mm)	K (Longshore Transport Coefficient)
Fine sand	Fine sand	0.063-0.2	200
Sand	Medium sand	0.2-0.63	100
Mixed sand/cobble	Coarse sand	0.63-2.0	50
Mixed sand/rock	Very coarse sand	<2.0	25 or less
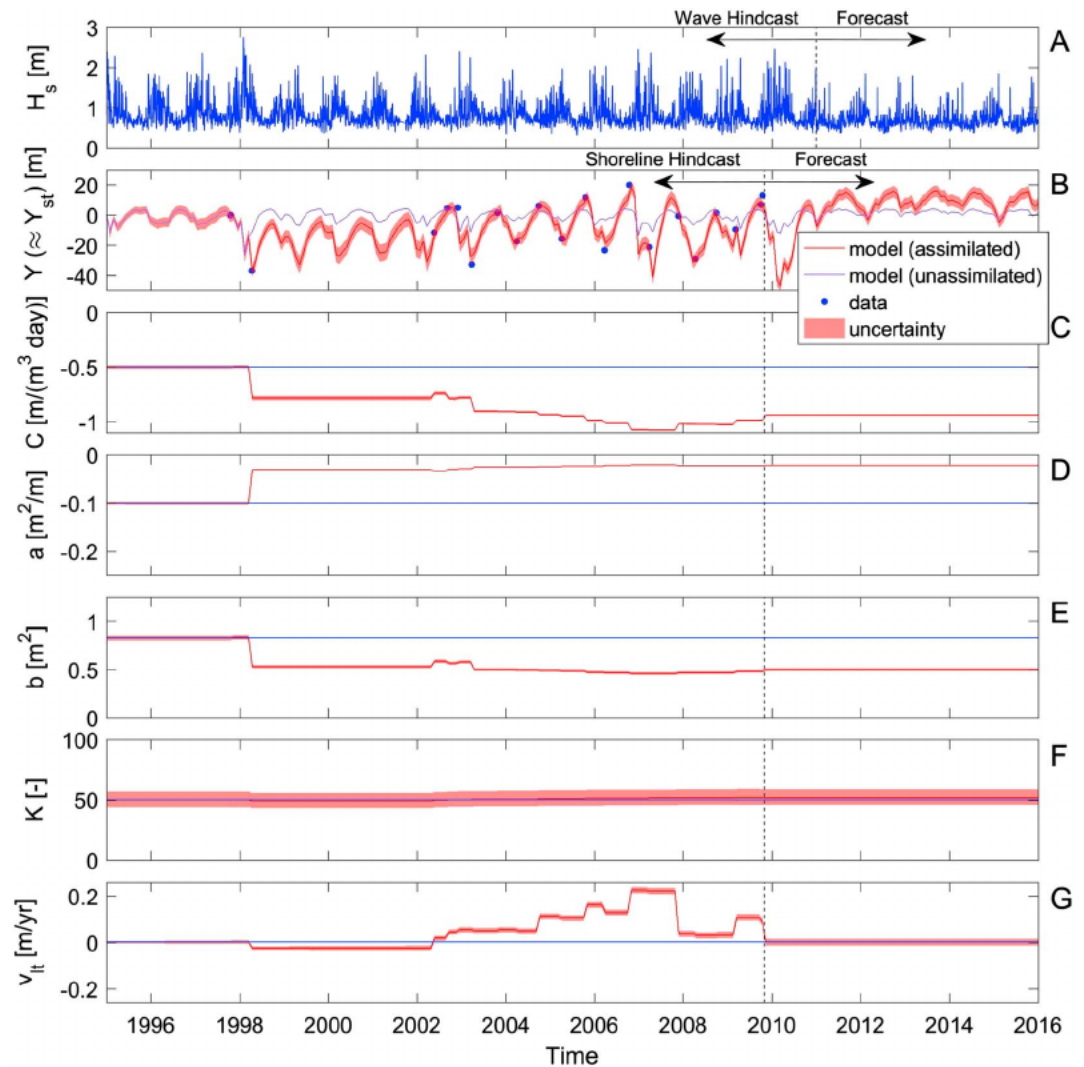
Figure 9. Time series of CoSMoS-COAST model predictions and parameters for transect #505 at La Jolla Shores. (a) Wave height time series, (b) simulated shoreline position, Y, with (red line) and without (purple line) data assimilation compared to the shoreline data (i.e., the intersection points of the transects and the shorelines, see Figure 6), and (c–g) initial (blue lines) and assimilated (red lines) model parameters.

magnitude. We expect smaller values for the assimilated rate (in Figure 8f) compared to the historical rate (Figure 7) because the dynamical processes of the CoSMoS-COAST model, i.e., the first three terms on the RHS of equation (1), should resolve a portion of the shoreline change signal.

Figure 9 shows the time series of wave height, shoreline position, and the assimilated parameters for the dynamical model at transect #505 near La Jolla Shores, CA. The initial and assimilated values of the shoreline position and model parameters are shown with the blue and red lines in Figure 9, respectively. The pink bands in Figure 9 represent the uncertainty in the assimilated values of the shoreline position and model parameters, which arise from the process noise estimates **P** and **Q** (discussed in Appendix B). The shoreline data, the intersection of transect #505, and the shoreline vectors (see, e.g., Figure 6b), are shown as blue dots in Figure 9b.

The wave height time series (Figure 9a) demonstrates a clear seasonal pattern of large wave heights in the winter and small wave heights in the summer. In response to the seasonal pattern in wave heights, the shoreline erodes during periods of large waves (i.e., winter) and recovers during periods of small waves (i.e., summer), as shown in Figure 9b. Note that the dynamical model aided by the data assimilation method (red line in Figure 9b) is able to reproduce the observed signal of seasonal shoreline change, as indicated by the good

Table 2. RMS Error Between Modeled and Observed Shoreline Position for Fall 2009 Shoreline

		RMS Shoreline Position Error	
	Average # of Shorelines	With Data Assimilation	Without Data Assimilation
All transects	12	14.5 m	20.7 m
South of Long Beach (transects 1–1946)	17	7.0 m	19.4 m
North of Long Beach (transects 1946–4802)	7	19.0 m	21.8 m

performance of the model compared to the shoreline observations particularly with regard to the extent of the maximally accreted and eroded beach states. On the other hand, the modeled shoreline change without using data assimilation (purple line in Figure 9b with the initial values of the model parameters shown in Figures 9c–9g) does not reproduce the observed shoreline change. In general, the performance of the unassimilated model is particularly poor when lacking good estimates for initial values of the model parameters, which are, of course, unknown a priori. Ultimately, the model's excellent performance during the hindcast period improves confidence that it may achieve a reliable quantitative prediction during the forecast period.

The wave forcing conditions (Figure 9a) transition from the hindcast period to the forecast period in 2011. The forecasted wave heights, derived from wind fields from the GDFL-ESM2M climate model [*Delworth et al.*, 2006] with the RCP 4.5 emissions scenario, are projected to decrease relative to the historical period for the low latitudes and mid-latitudes of the North Pacific such as Southern California [*Erikson et al.*, 2015]. Consequently, the standard deviation of the forecasted wave heights used in the current modeling application decreases by 18% on average relative to that of the hindcasted wave heights. This causes a muted seasonal shoreline erosion response (due to smaller seasonal wave heights) in 2011 following the transition from the hindcast period to the forecast period, as shown in Figure 9b. The modeled shoreline change, Y, shown in Figure 9b is dominated by the wave-driven cross-shore transport, $Y \approx Y_{st}$; and accordingly, the long-term components are almost negligible ($Y_{lt} \approx 0$) up to 2016. The dominance of the short-term shoreline change components was established in previous works [e.g., *Yates et al.*, 2009; *Doria et al.*, 2016] who demonstrated the strong performance of stand-alone equilibrium shoreline change models (i.e., Y_{st} only) for beaches in the region.

In Figures 9c–9g, we see that values of each model parameter are adjusted at each time step when shoreline data are available. Figure 9 does not depict the sea level response coefficient, $c = 1$, because data assimilation is turned off for this term as discussed in Appendix B. When no shoreline data is available, the value of the model parameter remains constant. Thus, after the last available shoreline observation is assimilated, the model parameters remain constant for the entire forecast period. Ideally, when enough data are available during the hindcast period, the assimilated values of the model parameters will be sufficiently converged before the forecast period begins. According to the analysis shown in Appendix C, this appears to be the case particularly for the equilibrium shoreline model parameters C, a, and b since these parameters are related to the short-term shoreline variability. The parameters representing the long-term shoreline behavior, on the other hand, K and v_{lt}, require longer records of shoreline data to obtain sufficient convergence [*Splinter et al.*, 2013].

We investigate the model's root-mean-square (RMS) error ($Y - Y_{obs}$) for the Fall 2009 shoreline, a data set that exists for all transects. The results of the RMS error with and without data assimilation are shown in Table 2. Data assimilation is able to reduce the RMS error by 30% for an average transect, by 64% for transects south of Long Beach, and by only 13% for transects North of Long Beach. The data assimilation method provides significant improvement for transects south of Long Beach because of the considerable amount of data available for the region.

After the dynamical simulations (1995–2100) are complete and validated, we plot the shoreline projections and uncertainties on a map in real-world coordinates. Figure 10 shows the initial shoreline position (green line) and the final (1 January 2100) shoreline position (red line) under the *National Research Council* [2012] sea level scenario. Figure 10 also shows yellow and red uncertainty bands representing the uncertainty in the shoreline position at 1 January 2100 estimated from the Kalman filter and the uncertainty due to *potential winter erosion* (defined as the maximally eroded beach state that is possible during winter months due to elevated wave heights and calculated as twice the standard deviation of Y_{st}), respectively. For many transects, the simulated shoreline position recedes up to or past the "non-erodible shoreline," which represents the interface between the sandy shoreline and coastal infrastructure. In the "hold the line" scenario shown in Figure 10, the shoreline is not allowed to erode past the non-erodible shoreline (black line) and into existing infrastructure. Under this
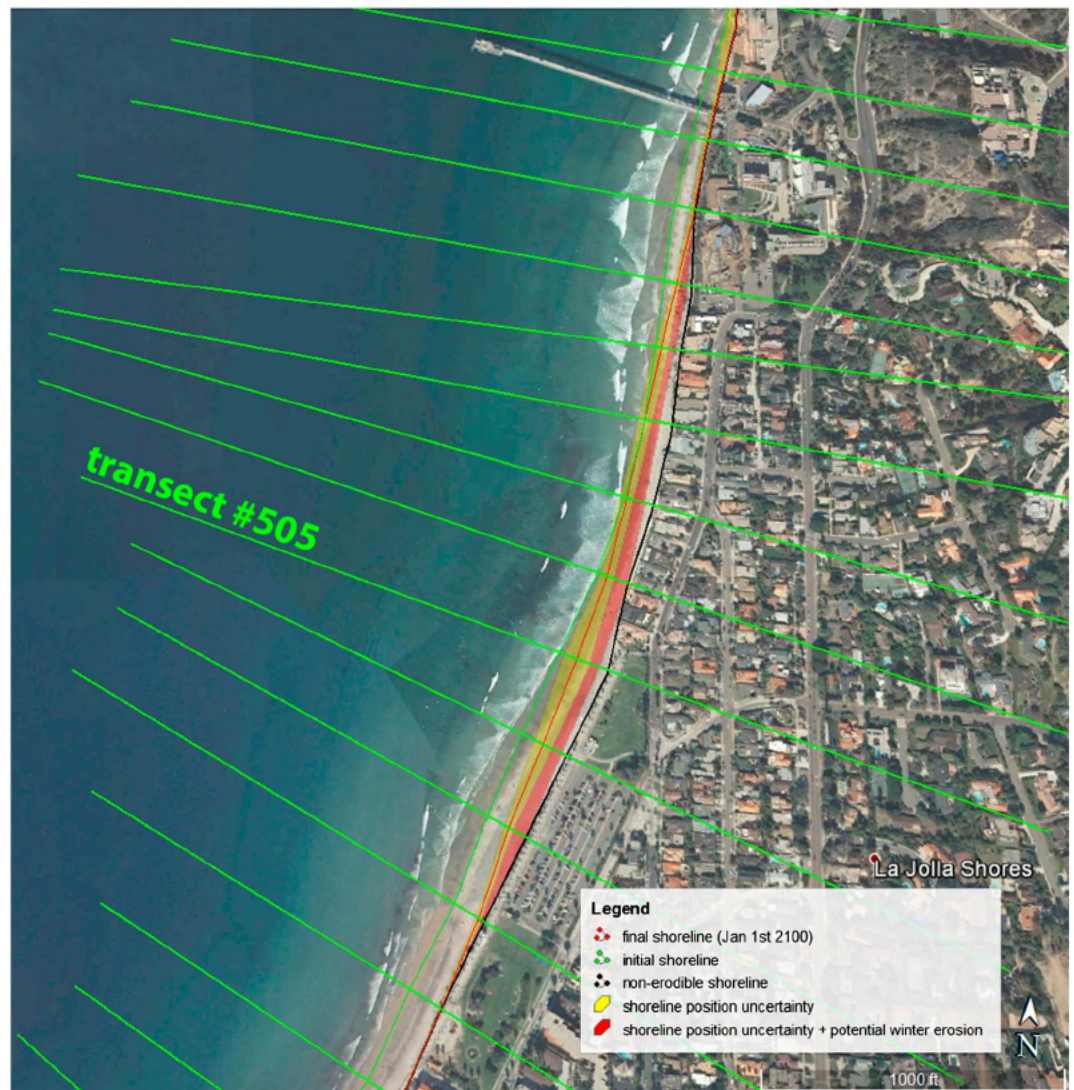
Figure 10. CoSMoS-COAST results for Southern California, pictured for La Jolla Shores. (Basemaps from Google Earth).

scenario, many of the transects experience complete beach loss by 2100 (e.g., the southern and northern ends of Figure 10). However, these results do not explicitly include cliff retreat and the resulting sediment supply to the beach. See Figure 12 for more details on beach loss in Southern California.

4.7. Uncertainty

Significant uncertainty is associated with resolved and unresolved coastal processes. The uncertainty bands presented in Figure 10 represent the process noise predicted by the Kalman filter (yellow bands) and the 95% confidence bands associated with the modeled shoreline fluctuations due to seasonal wave activity (red bands). Unresolved processes are implicitly accounted for in the uncertainty bands due to the estimated process noise in the Kalman filter. However, the lack of certainty in estimating the Kalman filter error covariance, P, and process noise, Q, may lead to more uncertainty than reported in these predictions. More details on the estimates of P and Q are given in Appendix B.

4.8. Computational Effort

Century-scale shoreline change simulations for the entire 500 km coast of Southern California using the developed model take approximately 15–20 min of computer time. On the other hand, century-scale, global-to-local nested WW3 and SWAN models require several days of computer time. Physics-based simulations of shoreline
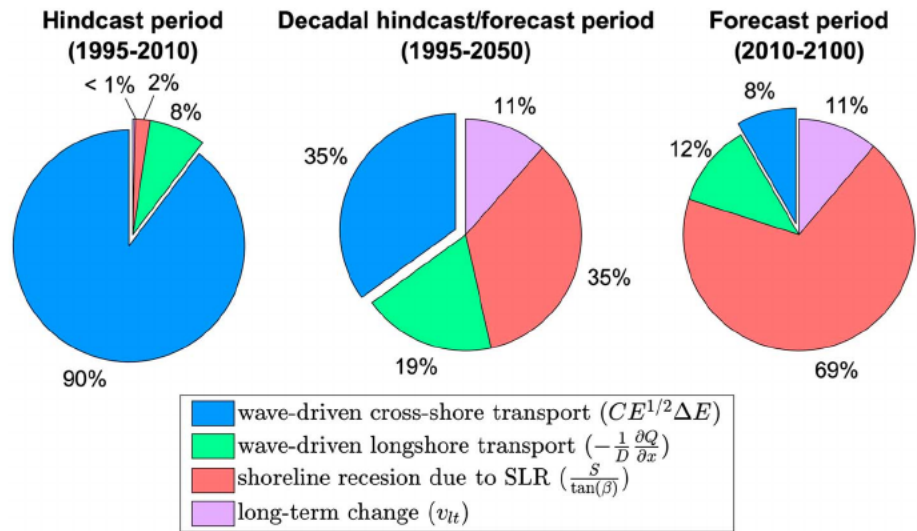
Figure 11. The relative contribution of each model component for different time periods.

change on such spatiotemporal scales are completely intractable due to accuracy, stability, and computational requirements. In the proposed model, data assimilation represents a computationally efficient means of estimating the model parameters since model calibration takes place over the course of a single model run. Traditional optimization techniques (e.g., Newton's method), on the other hand, may require several model runs to best estimate model parameters, thereby increasing computational cost. Short model run times such as the current shoreline model are necessary when evaluating a number of sea level and management scenarios. Models with lengthy run times become significantly less tractable when ensemble forcing conditions are applied.

4.9. Relative Contribution of Model Components

To evaluate the advantages of CoSMoS-COAST compared to individual process-based models, we measure the relative contributions of each model component, i.e., the four terms on the RHS of equation (1), to the overall shoreline change simulated under the *National Research Council* [2012] sea level scenario ($S = 0.93$ m by 2100). Figure 11 depicts the variance of the modeled shoreline change due to each individual term in the governing equation (equation (1)) relative to the variance of the total shoreline change, Y. For example, the variance of the wave-driven cross-shore transport is calculated as $\overline{\text{var}(Y_{st})}$, and its *relative contribution* to the model is calculated as $\overline{\text{var}(Y_{st})}/\overline{\text{var}(Y)}$, where var() calculates the variance of the time series and the overbar indicates an average over all of the "full model" transects, which retain all of the terms in equation (1).

Figure 11 depicts three different simulation periods (1995–2010, 1995–2050, and 2010–2100) of the "no hold the line, continued nourishment" scenario to evaluate the importance of each model component as a function of time. For the hindcast period (1995–2010), the modeled shoreline change is dominated by wave-driven cross-shore transport (90%) with little variance (10%) arising from longshore transport, long-term effects (v_{lt}), and the shoreline recession due to the negligible amount of SLR during this period. Many beaches in Southern California are dominated by cross-shore transport (particularly on interannual timescales) and thus are well simulated on short timescales using stand-alone equilibrium shoreline change models [*Yates et al.*, 2009; *Doria et al.*, 2016]. On the other hand, many northern beaches, e.g., Santa Barbara, experience oblique wave approaches and therefore longshore transport is a significant factor, especially evident after large fluvial discharge events [*Elias et al.*, 2009; *Barnard et al.*, 2009; *Barnard and Warrick*, 2010].

The modeled shoreline change for the forecast period (2010–2100) is primarily affected by the shoreline recession due to the large amount of SLR (0.93 m by 2100), which accounts for 69% of the model variance. For decadal-scale simulations (1995–2050), the modeled shoreline change is more uniformly distributed between cross-shore (35%) and longshore (19%) wave-driven transport and recession due to SLR (35%), with the remaining 11% driven by unresolved long-term effects. However, there is uncertainty associated with these percentages due to a number of different factors:

1. The long-term shoreline recession due to SLR dominates the long-term predictions, particularly when large sea level projections are applied. Increasing the projected sea level rise will proportionally increase the influence of the shoreline recession term, $S/\tan\beta$. The dominance the SLR term relies on the assumption that the Bruunian mechanism (or, perhaps more realistically, the passive flooding mechanism) holds. Although the constant of proportionality $(1/\tan\beta)$ is subject to considerable debate, it is very likely that SLR projections exceeding 1.0 m will dramatically reshape the world's coastline [*FitzGerald et al.*, 2008].

2. Changes in natural and anthropogenic sediment supply, e.g., the frequency of fluvial discharge events and beach nourishments, will affect the contribution of the long-term shoreline change rate term (v_{lt}).

3. Projections of decreased seasonal wave heights [*Erikson et al.*, 2015] will likewise decrease the relative importance of cross-shore wave-driven transport at long timescales.

4. Projections of counterclockwise rotations in wave angle associated with decreased North Pacific wave energy and increased South Pacific swell [*Erikson et al.*, 2015] may increase or decrease longshore transport in southern or northern beaches in Southern California, respectively.

5. The wave-driven cross-shore transport term oscillates about an equilibrium state, whereas the other terms often represent persistent trends. Thus, the variance due the long-term processes typically increases with time whereas the variance of the cross-shore wave-driven term remains relatively consistent. Consequently, the relative contributions of each term vary with time.

In summary, Figure 11 illustrates the clear advantage of the integrated approach used in CoSMoS-COAST over individual process-based models to simulate decadal-scale shoreline change in regions driven by nontrivial combinations of short- and long-term morphological processes. In contrast, individual processed-based shoreline models may miss a significant amount of the shoreline change signal, particularly for intermediate- and long-term predictions.

4.10. Summary of Projected Changes

The percentage of the transects in Southern California that experience total beach loss by 2050 and 2100 under the seven sea level scenarios (Figure 3) and four management scenarios is presented in Figure 12. The four management scenarios are (1) holding the line and no continued nourishment, (2) holding the line and continued nourishment, (3) no holding the line and no continued nourishment, and (4) no holding the line and continued nourishment. The results for the different sea level scenarios in Figure 12 apply the same color scheme as in Figure 3 to depict each scenario. Figures 12a and 12b show the percentage of transects whose final shoreline positions are eroded to within 1.0 m or past the non-erodible shoreline. Figures 12c and 12d show the percentage of transects whose final shoreline positions erode more than 5.0 m past the non-erodible shoreline. Note that only management scenarios 3 and 4 (no holding the line) are valid for the analysis presented in Figures 12c and 12d. The results in Figures 12a and 12b indicate that the model predicts that 9–21% and 31–59% of transects will experience beach loss by 2050 and 2100, respectively (under sea level scenarios of 0.93–2.0 m). Including seasonal erosion may increase these numbers to 25–39% and 45–67% of transects. The results in Figures 12c and 12d indicate that 3–11% and 22–53% of transects will erode more than 5.0 m beyond infrastructure by 2050 and 2100, respectively (under sea level scenarios of 0.93–2.0 m), and including seasonal erosion may increase these numbers to 25–39% and 40–65% of transects, respectively.

Overall, the model predictions in Figure 12 indicate that a substantial percentage of beaches in Southern California are susceptible to complete erosion. However, the proposed model is subject to many simplifying approximations, subjecting the predictions to considerable uncertainty. Nevertheless, based on the results in Figure 12, it is likely that at least 31% of Southern California will be completely eroded by 2100 in the absence of increased management efforts if SLR exceeds 1.0 m. The results also indicate that there is little overall difference between the nourished and unnourished management scenarios: the continued nourishment scenarios reduce the extent of erosion compared to the unnourished scenarios by at most 5% (see, e.g., Figure 12). However, for individual transects there can be significant differences between the shoreline responses to the two scenarios. The small differences among the management scenarios suggest that the current rate of beach nourishment is insufficient to deal with shoreline recession due to accelerated sea level rise. If future nourishments cannot keep pace with erosion, then the management practice of holding the line via shoreline armoring may become a critical issue in the overall evolution of the shoreline.
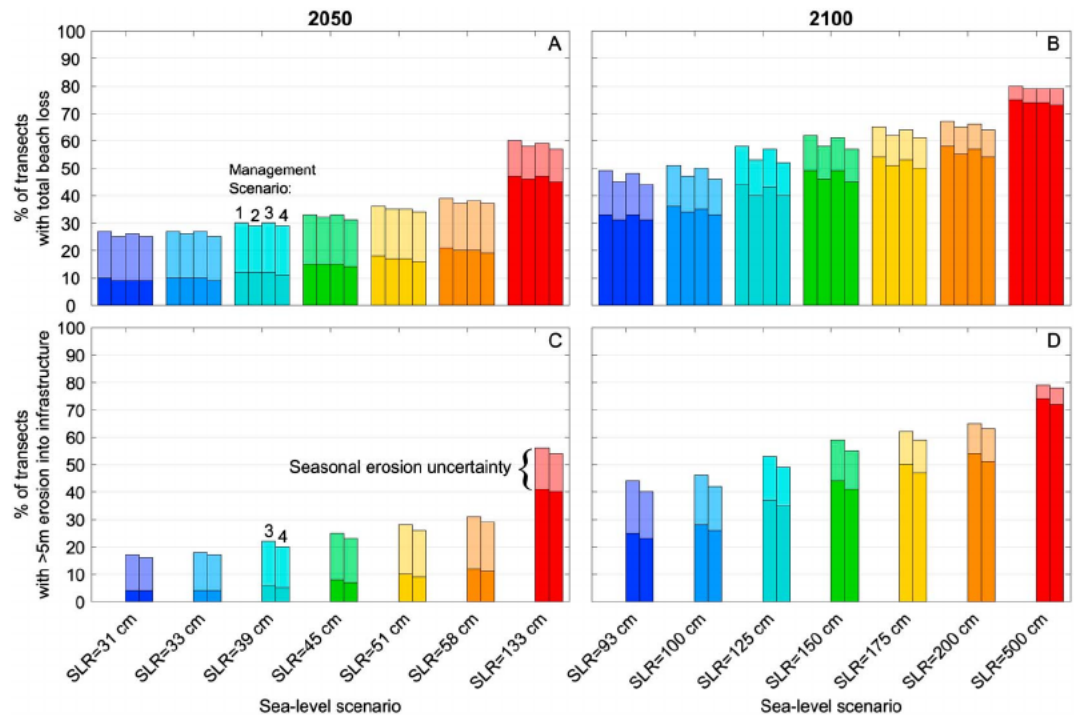
Figure 12. Summary of CoSMoS-COAST modeling results for the Southern California: The percentage of beach transects where the (a and b) model estimates total beach loss and (c and d) more than 5 m of erosion into cliffs and infrastructure in (a and c) 2050 and (b and d) 2100. The four management scenarios are (1) holding the line and no continued nourishment, (2) holding the line and continued nourishment, (3) no holding the line and no continued nourishment, and (4) no holding the line and continued nourishment.

The model predictions in Figure 12 suggest that there is significant potential for the shoreline to erode past the back beach and into existing infrastructure. The shoreline model does not account for erosion through different substrates (e.g., rocky cliffs and concrete structures) but instead treats the entire transect as a sandy substrate. Clearly, this approach will overestimate the amount of erosion into cliffs and infrastructure under management scenarios 3 and 4 (not holding the line). However, the model predictions should remain valid until this fully eroded state occurs. Ultimately, the possibility of reaching such a fully eroded state might be considered unacceptable and therefore encourage new management practices and nourishment efforts. In this case, the model's long-term shoreline change rate term might be specified to explore a range of nourishment intervention scenarios.

5. Conclusions

We have developed a flexible and multifaceted model to predict long-term shoreline change across a wide variety of geomorphic settings under the name of CoSMoS-COAST, the Coastal One-line Assimilated Simulation Tool. For the first time, the model applies a synthesis of individual process-based shoreline change models, each resolving unique and addable components of shoreline change, e.g., longshore and cross-shore transport. Because manual parameter tuning is infeasible on large spatiotemporal scales, the model uses data assimilation to automatically calibrate the model parameters from sparse, noisy signals of observed historical shoreline change. Ultimately, we use data assimilation as a tool to improve the confidence in long-term predictions. The proposed model is applied to simulate shoreline change on 500 km of Southern California coastline. The model predictions, although subjected to considerable uncertainty, indicate that significant impacts to the shoreline will occur due to accelerated sea level rise, with 31% to 67% of beaches in Southern California lost by 2100 under the 0.93 to 2.0 m SLR projections. The simulation results indicate that current rates of beach nourishment may be insufficient to keep pace with potential long-term erosion. It is likely that beaches in Southern California will require substantial management efforts (e.g., nourishments and armoring) to maintain beach widths and prevent impacts to coastal infrastructure.

Appendix A: Longshore Transport Model

This appendix details the longshore transport model. The numerical method for longshore transport used in COSMOS-COAST follows *Vitousek and Barnard* [2015]. The shoreline position (in real-world coordinates x, y) at any time step is given by

$$x_k^n = x_k^0 + Y_k^n \cos(\phi_k), \tag{A1}$$

$$y_k^n = y_k^0 + Y_k^n \sin(\phi_k). \tag{A2}$$

Thus, the shoreline position is constrained to transect k with shore-normal angle, ϕ_k. In other words, the shoreline moves as if "on rails." Coordinates (x_k^0, y_k^0) represent the location of the onshore end of the transect, and Y_k^n represents the distance from the transect end (x_k^0, y_k^0) to the shoreline (x_k^n, y_k^n). The alongshore distance between transects can be calculated by

$(\Delta X)_k = \frac{1}{2}\left(\sqrt{(x_{k+1} - x_k)^2 + (y_{k+1} - y_k)^2} + \sqrt{(x_k - x_{k-1})^2 + (y_k - y_{k-1})^2} \right)$ as either a time-varying quantity (using values with time index n) or fixed quantity (using time index $n = 0$).

The numerical method begins with equation (5). The alongshore transport rate following equation (2) is calculated numerically by

$$Q_{k+1/2}^{n+1/2} = (Q_0)_{k+1/2}^{n+1/2} \sin\left(2\alpha_{k+1/2}^{n+1/2}\right). \tag{A3}$$

The angle $\alpha_{k+1/2}^{n+1/2}$ is calculated as

$$\alpha_{k+1/2}^{n+1/2} = (\alpha_{\text{wave}})_{k+1/2}^{n+1/2} - (\alpha_{\text{shoreline}})_{k+1/2}^{n+\theta}, \tag{A4}$$

where $(\alpha_{\text{wave}})_{k+1/2}^{n+1/2}$ is the incident wave angle obtained from a nearshore model (e.g., SWAN) and

$$(\alpha_{\text{shoreline}})_{k+1/2}^{n+\theta} = \text{atan2}\left(y_{k+1}^{n+\theta} - y_k^{n+\theta}, x_{k+1}^{n+\theta} - x_k^{n+\theta}\right). \tag{A5}$$

The superscript $n + \theta$ in equation (A5) implies

$$x_k^{n+\theta} = \theta x_k^{n+1} + (1 - \theta) x_k^n, \tag{A6}$$

$$y_k^{n+\theta} = \theta y_k^{n+1} + (1 - \theta) y_k^n. \tag{A7}$$

The parameter θ ($0 \leq \theta \leq 1$) determines the temporal discretization of the numerical method. For example, if $\theta = 0$ then the time stepping method is the (explicit) forward Euler method. $\theta = 1$ is the (implicit) backward Euler method, and $\theta = \frac{1}{2}$ is the trapezoidal method (a semi-implicit method for the shallow water equations, see, e.g., *Casulli and Cattani* [1994]). We can interpret the temporal discretization in equations (A5)–(A7) in the following way: The shoreline angle $(\alpha_{\text{shoreline}})_{k+1/2}^{n+\theta}$ is computed as weighted average of the current shoreline position (x_k^n, y_k^n) and the future shoreline position (x_k^{n+1}, y_k^{n+1}) with the weighting factor θ.

Substituting equations (A1) and (A2) into equations (A6) and (A7), respectively, we obtain

$$x_k^{n+\theta} = x_k^0 + \left(\theta Y_k^{n+1} + (1 - \theta) Y_k^n\right) \cos(\phi_k) = x_k^0 + Y_k^{n+\theta} \cos(\phi_k), \tag{A8}$$

$$y_k^{n+\theta} = y_k^0 + \left(\theta Y_k^{n+1} + (1 - \theta) Y_k^n\right) \sin(\phi_k) = y_k^0 + Y_k^{n+\theta} \sin(\phi_k). \tag{A9}$$

This method is implicit (when $\theta > 0$) because the solution that we seek, Y_k^{n+1}, is a function of itself via equation (5) and subsequent relationships (A3)–(A5), (A8), and (A9) which contain Y_k^{n+1}. If $\theta = 0$, then the method is explicit since Y_k^{n+1} depends entirely on Y_k^n (and not Y_k^{n+1}) in equations (A8) and (A9).

In vector notation, equation (5) (with equations (A3)–(A5), and (A9)) are written as

$$\mathbf{F}\left(\mathbf{Y}^{n+1}\right) = \mathbf{0}, \tag{A10}$$

for the vector of unknown shoreline positions $\mathbf{Y}^{n+1} = \left[Y_1^{n+1}, Y_2^{n+1}, Y_3^{n+1}, \ldots, Y_k^{n+1}, \ldots, Y_{N-1}^{n+1}, Y_N^{n+1}\right]^T$, where N is the total number of shore-normal transects and superscript T represents the transpose. The system of equation (A10) is nonlinear due to the presence of the sine and arctangent functions. If equation (A10) was simplified by retaining the first terms in a Taylor series of sine and arctangent, then the system of

equations could be assembled into a linear system of equations (e.g., $\mathbf{A}\mathbf{Y}^{n+1} = \mathbf{b}$). The nonlinear system of equation (A10) can be solved using a variety of methods (e.g., Newton-Raphson method). Following *Vitousek and Barnard* [2015], we use Jacobian-Free Newton-Krylov method (see, e.g., *Knoll and Keyes* [2004]) in order to (as the name implies) eliminate the need to derive the Jacobian matrix of equation (A10).

Appendix B: Data Assimilation

In this appendix, we discuss the modification of the model equations in order to preserve the expected signs of the model parameters during data assimilation step. As mentioned previously, parameters C and a are negative, and b, c, and K are positive. However, there is no guarantee that the data assimilation method, described in section 3, will preserve the expected signs of the parameters.

We modify the parameters C_k and a_k in equation (4) according to

$$
\begin{aligned}
\frac{(Y_{st})_k^{n+1} - (Y_{st})_k^n}{\Delta t} &= C_k \left(E_k^n\right)^{1/2} \left(E_k^n - a_k (Y_{st})_k^n - b_k\right) \\
&= -C_k^+ \left(E_k^n\right)^{1/2} \left(E_k^n - -a_k^+ (Y_{st})_k^n - b_k^+\right) \\
&= -\left(E_k^n\right)^{1/2} \left(C_k^+ E_k^n + C^+ a_k^+ (Y_{st})_k^n - C_k^+ b\right),
\end{aligned}
\tag{B1}
$$

where $C_k^+ = -C_k$ and $a_k^+ = -a_k$ are the positive values of C_k and a_k, respectively, and k is the transect index. Thus, all parameters $C_k^+, a_k^+, b_k, c_k, K_k$ in the governing equations are positive. We will also absorb the coefficients and redefine the parameters of equation (B1) as

$$
\frac{(Y_{st})_k^{n+1} - (Y_{st})_k^n}{\Delta t} = -\left(E_k^n\right)^{1/2} \left(C_k^+ E_k^n + A_k (Y_{st})_k^n - B_k\right),
\tag{B2}
$$

where $A_k = C_k^+ a_k^+$ and $B_k = C_k^+ b_k$. The goal of this modification is to reduce the interdependence of the parameters C_k, a_k, and b_k during the data assimilation step. Following this step, all model parameters, $C_k^+, A_k, B_k, c_k, K_k$ are positive for each transect k.

Now, we will replace the model parameters in equations (4) and (5) with

$$
C_k^+ = \left(C_0^+\right)_k \exp\left(\sigma_C (C_1)_k\right)
\tag{B3}
$$

$$
A_k = (A_0)_k \exp\left(\sigma_A (A_1)_k\right)
\tag{B4}
$$

$$
B_k = (B_0)_k \exp\left(\sigma_B (B_1)_k\right)
\tag{B5}
$$

$$
c_k = (c_0)_k \exp\left(\sigma_c (c_1)_k\right)
\tag{B6}
$$

$$
K_k = (K_0)_k \exp\left(\sigma_K (K_1)_k\right)
\tag{B7}
$$

where $\left(C_0^+\right)_k = -(C_0)_k$, $(A_0)_k = \left(C_0^+\right)_k \left(a_0^+\right)_k = (C_0)_k (a_0)_k$, $(B_0)_k = \left(C_0^+\right)_k (b_0)_k = -(C_0)_k (b_0)_k$, and $(C_0)_k, (a_0)_k, (b_0)_k, (c_0)_k, (K_0)_k$ are the initial values of the parameters C_k, a_k, b_k, c_k, K_k, respectively. The static parameters $\sigma_C, \sigma_A, \sigma_B, \sigma_c, \sigma_K$ (typically, all set to a nominal value of 0.5) influence the range of the possible values of the assimilated parameters.

After substituting the modified parameter equations (B3)–(B7) into the model equations (5) and (B2), the model equations become

$$
\frac{(Y_{st})_k^{n+1} - (Y_{st})_k^n}{\Delta t} = -\left(E_k^n\right)^{1/2} \left(\left(C_0^+\right)_k \exp\left(\sigma_C (C_1)_k\right) E_k^n + (A_0)_k \exp\left(\sigma_A (A_1)_k\right) (Y_{st})_k^n - (B_0)_k \exp\left(\sigma_B (B_1)_k\right)\right),
\tag{B8}
$$

$$
\frac{(Y_{lt})_k^{n+1} - (Y_{lt})_k^n}{\Delta t} = -\frac{(K_0)_k \exp\left(\sigma_K (K_1)_k\right)}{d_k} \frac{Q_{k+1/2}^{n+\theta} - Q_{k-1/2}^{n+\theta}}{(\Delta X)_k} - \frac{(c_0)_k \exp\left(\sigma_c (c_1)_k\right)}{\tan\beta_k} \left(\frac{\partial S}{\partial t}\right)_k^n + (v_{lt})_k.
\tag{B9}
$$

The state vector used in data assimilation is

$$
\boldsymbol{\psi}_k = \left[(Y_{lt})_k \ (v_{lt})_k \ (Y_{st})_k \ (C_1)_k \ (A_1)_k \ (B_1)_k \ (c_1)_k \ (K_1)_k \right]^T.
$$

So thus, the modified method assimilates the parameters $(C_1)_k, (A_1)_k, (B_1)_k, (c_1)_k, (K_1)_k$, and the parameters C_k, a_k, b_k, c_k, K_k will have their requisite sign.

The exponential functions in (B3)–(B7) serve two purposes: (1) $\exp(x)$ is positive for real (i.e., positive or negative) values of x ensuring the requisite signs of the parameters during data assimilation, and (2) it is easy to obtain derivatives of this function (since $\frac{d\exp(x)}{dx} = \exp(x)$) when calculating the Jacobian, $J_{ij} = \frac{\partial F_i}{\partial \psi_j}$, of the data assimilation method.

The only nontrivial and nondiagonal entries of the Jacobian will be $\frac{\partial F_1}{\partial \psi_j}$ and $\frac{\partial F_3}{\partial \psi_j}$, where

$$F_1 = (Y_{lt})_k^n - \Delta t \frac{(K_0)_k \exp(\sigma_K(K_1)_k)}{d_k} \frac{Q_{k+1/2}^{n+\theta} - Q_{k-1/2}^{n+\theta}}{(\Delta X)_k} - \Delta t \frac{(c_0)_k \exp(\sigma_c(c_1)_k)}{\tan\beta_k} \left(\frac{\partial S}{\partial t}\right)_k^n + \Delta t (v_{lt})_k$$

$$F_3 = (Y_{st})_k^n - \Delta t (E_k^n)^{1/2} \left((C_0^+)_k \exp(\sigma_C(C_1)_k) E_k^n + (A_0)_k \exp(\sigma_A(A_1)_k)(Y_{st})_k^n - (B_0)_k \exp(\sigma_B(B_1)_k) \right).$$

So thus, $J_{ij} = I$, where I is the identity matrix and

$$J_{1j} = \frac{\partial F_1}{\partial \psi_j} = \begin{bmatrix} 1 & \Delta t & 0 & 0 & 0 & 0 & -\Delta t \frac{(c_0)_k \sigma_c \exp(\sigma_c(c_1)_k)}{\tan\beta_k} \left(\frac{\partial S}{\partial t}\right)_k^n & -\Delta t \frac{(K_0)_k \sigma_K \exp(\sigma_K(K_1)_k)}{d_k} \frac{Q_{k+1/2}^{n+\theta} - Q_{k-1/2}^{n+\theta}}{(\Delta X)_k} \end{bmatrix}$$

$$J_{3j} = \frac{\partial F_3}{\partial \psi_j} = \begin{bmatrix} 0 & 0 & 1 - \Delta t (E_k^n)^{1/2}(A_0)_k \exp(\sigma_A(A_1)_k) & -\Delta t (E_k^n)^{1/2}\left((C_0^+)_k \sigma_C \exp(\sigma_C(C_1)_k) E_k^n \right) \dots \\ -\Delta t (E_k^n)^{1/2}((A_0)_k \sigma_A \exp(\sigma_A(A_1)_k)(Y_{st})_k^n & \Delta t (E_k^n)^{1/2}((B_0)_k \sigma_B \exp(\sigma_B(B_1)_k)) & 0 & 0 \end{bmatrix}.$$

For the Southern California application, the initial error covariance matrix, process noise, and measurement error are given by

$$\mathbf{P} = \text{diag}\left(\begin{bmatrix} 1 & 2\times10^{-4} & 1 & 0.25 & 0.25 & 0.25 & 1\times10^{-10} & 0.25 \end{bmatrix}\right)^2,$$

$$\mathbf{Q} = \text{diag}\left(\begin{bmatrix} 0.1 & 1\times10^{-5} & 0.1 & 1\times10^{-3} & 1\times10^{-3} & 1\times10^{-3} & 1\times10^{-10} & 1\times10^{-4} \end{bmatrix}\right)^2,$$

and

$$\mathbf{R} = 1\text{m},$$

respectively, for each "full model" transect. We selected the values of $\mathbf{P}$ and $\mathbf{Q}$ for Y_{st}, v_{lt} and Y_{lt} to be consistent with *Long and Plant* [2012], since these terms are unaffected by the modified Kalman filter method. However, the values of $\mathbf{P}$ and $\mathbf{Q}$ associated with C_1, A_1, B_1, c_1, K_1 become harder to interpret since they relate to the process noise of the original coefficients C, a, b, c, K via equations (B3)–(B7). We made a number of sensitivity tests to different values of $\mathbf{P}$ and $\mathbf{Q}$, ultimately settling on the numbers reported above, which correspond to reasonable values of uncertainty in the original coefficients. We note that the $\mathbf{P}$ and $\mathbf{Q}$ values associated with the Bruunian response coefficient, c, are set to very small values ($\mathbf{P}_{7,7} = \mathbf{Q}_{7,7} = 1\times10^{-10}$) in order to effectively turn off data assimilation associated with this term. We chose to prevent data assimilation of the Bruunian response term since sea level rise on the U.S. West Coast was negligible compared to the global mean during the hindcast period (1995–2010) due to dynamical factors [*Bromirski et al.*, 2011]. Thus, changes to the assimilated value of c would, most likely, be physically unrealistic. Similarly, we effectively turn off both the model terms and the data assimilation method associated with the longshore and cross-shore wave-driven transport processes on "cross-shore only" and "rate only" transects by setting $K = 0$; $\mathbf{P}_{8,8} = \mathbf{Q}_{8,8} = 1\times10^{-10}$ and $K = C = 0$; $\mathbf{P}_{4,4} = \mathbf{Q}_{4,4} = \mathbf{P}_{8,8} = \mathbf{Q}_{8,8} = 1\times10^{-10}$, respectively.

Appendix C: Convergence of Model Parameters

We examine the convergence of the model parameters (C, a, b, K, v_{lt}) as a function of the number of shoreline observations, n. As more observations are assimilated (increasing n), the difference between successive estimates of the model parameters, $\psi^{n+1} - \psi^n$, decreases. Figure C1 illustrates the average convergence rate for each model parameter according to $\left|\frac{\psi^{n+1} - \psi^n}{\psi^0}\right|$ (or $|\psi^{n+1} - \psi^n|$ if $\psi^0 = 0$, which is the case for $\psi = v_{lt}$). Figure C1 depicts the average rate of convergence (blue lines) and the overall trend (black dashed line) for transects #1–1946 (South of Long Beach), where an average of 17 shoreline vectors are available to assimilate. The axes in Figure C1 are on logarithmic scales, and thus, the (roughly linear) decreasing trends correspond to asymptotic convergence of the model parameters. As shown in Figure C1, the model parameters do converge; however, the convergence is not monotonic, likely due to the variable nature of $Y_{obs}^{n+1} - Y_{modeled}^*$ (the difference between observed and modeled shoreline positions) in step (5) of the data assimilation method. As shown in Figures C1a–C1c, the short-term shoreline change parameters (C, a, b) converge rapidly. This result is expected as parameters C, a, b govern the behavior of wave-driven seasonal variability, a process that is
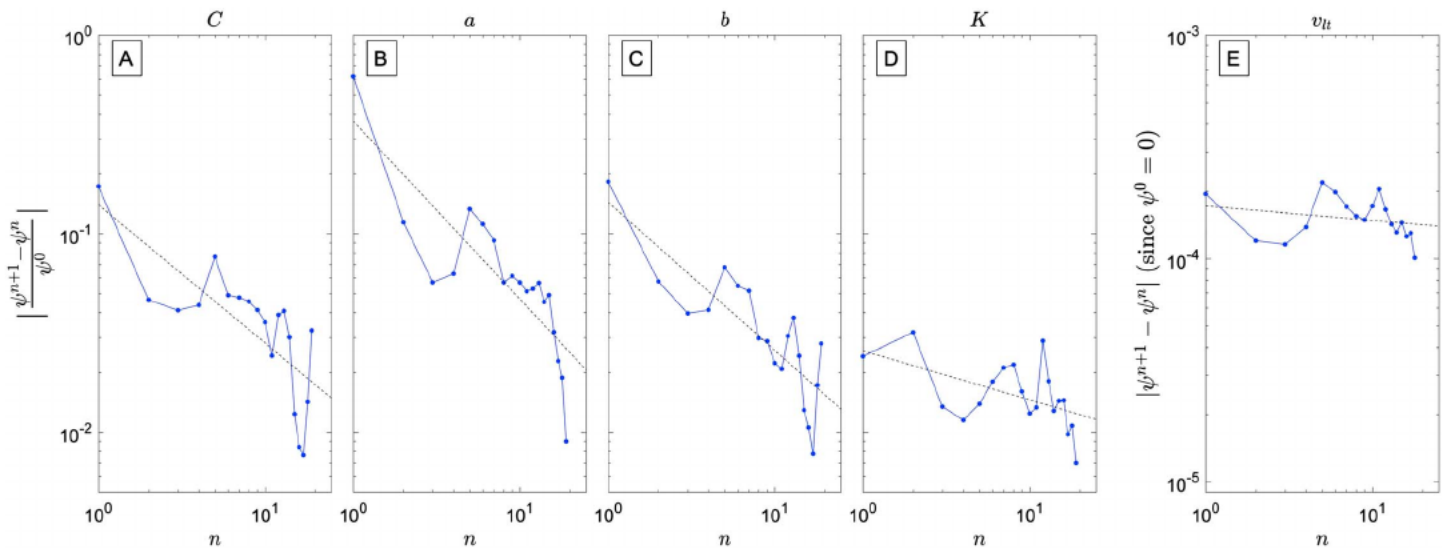
Figure C1. Convergence of the model parameters via data assimilation.

well resolved with 10–15 years of available data. On the other hand, the long-term shoreline change parameters K and v_{lt} converge slower, likely due to the limited temporal extent of the available shoreline data relative to the long timescales of variability associated with these parameters.

References

Anderson, T. R., C. H. Fletcher, M. M. Barbee, L. N. Frazer, and B. M. Romine (2015), Doubling of coastal erosion under rising sea level by mid-century in Hawaii, *Nat. Hazards*, *78*(1), 75–103.

Antolínez, J. A. A., F. J. Méndez, P. Camus, S. Vitousek, E. M. González, P. Ruggiero, and P. Barnard (2015), A multi-scale climate emulator for long-term morphodynamics (MUSCLE-morpho), *J. Geophys. Res. Oceans*, *121*, 775–791, doi:10.1002/2015JC011107.

Ashton, A., A. B. Murray, and O. Arnoult (2001), Formation of coastline features by large-scale instabilities induced by high-angle waves, *Nature*, *414*(6861), 296–300.

Ashton, A. D., and A. B. Murray (2006), High-angle wave instability and emergent shoreline shapes: 1. Modeling of sand waves, flying spits, and capes, *J. Geophys. Res.*, *111*, F04011, doi:10.1029/2005JF000422.

Banno, M., and Y. Kuriyama (2014), Prediction of future shoreline change with sea-level rise and wave climate change at Hasaki, Japan, *Coast. Eng. Process.*, *1*(34), 56.

Barnard, P.L., et al. (2009), Coastal processes study of Santa Barbara and Ventura counties, California, *U.S. Geol. Surv. Open File Rep.*, *2009-1029*, 926.

Barnard, P. L., and J. A. Warrick (2010), Dramatic beach and nearshore morphological changes due to extreme flooding at a wave-dominated river mouth, *Mar. Geol.*, *271*(1), 131–148.

Barnard, P. L., M. van Ormondt, L. H. Erikson, J. Eshleman, C. Hapke, P. Ruggiero, P. N. Adams, and A. C. Foxgrover (2014), Development of the Coastal Storm Modeling System (CoSMoS) for predicting the impact of storms on high-energy, active-margin coasts, *Nat. Hazards*, *74*(2), 1095–1125.

Barnard, P. L., et al. (2015), Coastal vulnerability across the Pacific dominated by El Niño/Southern Oscillation, *Nat. Geosci.*, *8*(10), 801–807.

Bauer, B. O., R. G. D. Davidson-Arnott, P. A. Hesp, S. L. Namikas, J. Ollerhead, and I. J. Walker (2009), Aeolian sediment transport on a beach: Surface moisture, wind fetch, and mean transport, *Geomorphology*, *105*(1), 106–116.

Booij, N., R. C. Ris, and L. H. Holthuijsen (1999), A third-generation wave model for coastal regions: 1. Model description and validation, *J. Geophys. Res.*, *104*(C4), 7649–7666, doi:10.1029/98JC02622.

Bromirski, P. D., A. J. Miller, R. E. Flick, and G. Auad (2011), Dynamical suppression of sea level rise along the Pacific coast of North America: Indications for imminent acceleration, *J. Geophys. Res.*, *116*, C07005, doi:10.1029/2010jc006759.

Bruun, P. (1962), Sea-level rise as a cause of shore erosion, *J. Waterw. Harb.Div.*, *88*(1), 117–132.

Bruun, P. (1988), The Bruun rule of erosion by sea-level rise: A discussion on large-scale two-and three-dimensional usages, *J. Coast. Res.*, 627–648.

Castelle, B., and G. Coco (2013), Surf zone flushing on embayed beaches, *Geophys. Res. Lett.*, *40*, 2206–2210, doi:10.1002/grl.50485.

Casulli, V., and E. Cattani (1994), Stability, accuracy and efficiency of a semi-implicit method for three-dimensional shallow water flow, *Comput. Math. Appl.*, *27*(4), 99–112.

Coastal Data Information Program (2016), Scripps Institution of Oceanography, Integrative Oceanography Division, San Diego, Calif. [Available at http://cdip.ucsd.edu.]

Coco, G., N. Senechal, A. Rejas, K. R. Bryan, S. Capo, J. P. Parisot, J. A. Brown, and J. H. MacMahan (2014), Beach response to a sequence of extreme storms, *Geomorphology*, *204*, 493–501.

Cooper, J. A. G., and O. H. Pilkey (2004), Sea-level rise and shoreline retreat: Time to abandon the Bruun rule, *Global Planet. Change*, *43*(3), 157–171.

Church, J. A., et al. (2013), Sea level change, in *Climate Change 2013: The Physical Science Basis. Contribution of Working Group I to the Fifth Assessment Report of the Intergovernmental Panel on Climate Change*, edited by T. F. Stocker et al., Cambridge Univ. Press, Cambridge, U. K., and New York.

Crowell, M., S. P. Leatherman, and M. K. Buckley (1991), Historical shoreline change: Error analysis and mapping accuracy, *J. Coast. Res.*, 839–852.

Daly, C. J., K. R. Bryan, J. A. Roelvink, A. H. F. Klein, D. Hebbeln, and C. Winter (2011), Morphodynamics of embayed beaches: The effect of wave conditions, *J. Coast. Res.*, *64*, 1003.

Davidson-Arnott, R. G. (2005), Conceptual model of the effects of sea level rise on sandy coasts, *J. Coast. Res.*, 1166–1172.

Davidson, M. A., R. P. Lewis, and I. L. Turner (2010), Forecasting seasonal to multi-year shoreline change, *Coast. Eng.*, *57*(6), 620–629.

Davidson, M. A., K. D. Splinter, and I. L. Turner (2013), A simple equilibrium model for predicting shoreline change, *Coast. Eng.*, *73*, 191–202.

Delworth, T. L., et al. (2006), GFDL's CM2 global coupled climate models. Part I: Formulation and simulation characteristics, *J. Clim.*, *19*(5), 643–674.

de Winter, R. C., F. Gongriep, and B. G. Ruessink (2015), Observations and modeling of alongshore variability in dune erosion at Egmond aan Zee, the Netherlands, *Coast. Eng.*, *99*, 167–175.

Dolan, R., B. Hayden, and J. Heywood (1978), A new photogrammetric method for determining shoreline erosion, *Coast. Eng.*, *2*, 21–39.

Doria, A., R. T. Guza, W. C. O'Reilly, and M. L. Yates (2016), Observations and modeling of San Diego beaches during El Niño, *Cont. Shelf Res.*, *124*, 153–164.

Elias, E. P. L., P. L. Barnard, and J. Brocatus (2009), Littoral transport rates in the Santa Barbara littoral cell: A process-based model analysis, *J. Coast. Res.*, *56*, 947–951.

Erikson, L. H., C. A. Hegermiller, P. L. Barnard, P. Ruggiero, and M. van Ormondt (2015), Projected wave conditions in the Eastern North Pacific under the influence of two CMIP5 climate scenarios, *Ocean Model.*, *96*, 171–185.

Falqués, A. (2003), On the diffusivity in coastline dynamics, *Geophys. Res. Lett.*, *30*(21), 2119, doi:10.1029/2003GL017760.

FitzGerald, D. M., M. S. Fenster, B. Argow, and I. V. Buynevich (2008), Coastal impacts due to sea-level rise, *Annu. Rev. Earth Planet. Sci.*, *36*, 601–647.

Fletcher, C., J. Rooney, M. Barbee, S. C. Lim, and B. Richmond (2003), Mapping shoreline change using digital orthophotogrammetry on Maui, Hawaii, *J. Coast. Res.*, 106–124.

Flick, R. E. (1993), The myth and reality of Southern California beaches, *Shore Beach*, *61*(3), 3–13.

French, J., A. Payo, B. Murray, J. Orford, M. Eliot, and P. Cowell (2016), Appropriate complexity for the prediction of coastal and estuarine geomorphic behaviour at decadal to centennial scales, *Geomorphology*, *256*, 3–16.

Gallop, S. L., K. R. Bryan, G. Coco, and S. A. Stephens (2011), Storm-driven changes in rip channel patterns on an embayed beach, *Geomorphology*, *127*(3), 179–188.

Hansen, J. E., and P. L. Barnard (2010), Sub-weekly to interannual variability of a high-energy shoreline, *Coast. Eng.*, *57*(11), 959–972.

Hapke, C. J., D. Reid, B. M. Richmond, P. Ruggiero, and J. List (2006), National assessment of shoreline change Part 3: Historical shoreline change and associated coastal land loss along sandy shorelines of the California Coast, *U.S. Geol. Surv. Open File Rep.*, *1219*, 27.

Harley, M. D., I. L. Turner, and A. D. Short (2015), New insights into embayed beach rotation: The importance of wave exposure and cross-shore processes, *J. Geophys. Res. Earth*, *120*(8), 1470–1484.

Hegermiller, C. A., L. H. Erikson, and P. L. Barnard (2016), Nearshore waves in Southern California: Hindcast, and modeled historical and 21st-century projected time series: U.S. Geological Survey data release. [Available at 10.5066/F7N29V2V.]

Hemer, M. A., et al. (2013), Projected changes in wave climate from a multi-model ensemble, *Nat. Clim. Change*, *3*(5), 471–476.

Hurst, M. D., A. Barkwith, M. A. Ellis, C. W. Thomas, and A. B. Murray (2015), Exploring the sensitivities of crenulate bay shorelines to wave climates using a new vector-based one-line model, *J. Geophys. Res. Earth*, *3*, 471–476, doi:10.1038/nclimate1791.

Knoll, D. A., and D. E. Keyes (2004), Jacobian-free Newton–Krylov methods: A survey of approaches and applications, *J. Comput. Phys.*, *193*(2), 357–397.

Inman, D. L., and S. A. Jenkins (1999), Climate change and the episodicity of sediment flux of small California Rivers, *J. Geol.*, *107*(3), 251–270.

Kaergaard, K., and J. Fredsoe (2013), A numerical shoreline model for shorelines with large curvature, *Coast. Eng.*, *74*, 19–32.

Larson, M., H. Hanson, and N. C. Kraus (1997), Analytical solutions of one-line model for shoreline change near coastal structures, *J. Waterw. Port Coast. Ocean Eng.*, *123*(4), 180–191.

Limber, P. W., and A. B. Murray (2011), Beach and sea-cliff dynamics as a driver of long-term rocky coastline evolution and stability, *Geology*, *39*(12), 1147–1150.

Limber, P. W., A. Brad Murray, P. N. Adams, and E. B. Goldstein (2014), Unraveling the dynamics that scale cross-shore headland relief on rocky coastlines: 1. Model development, *J. Geophys. Res. Earth*, *119*, 854–873.

Limber, P., P. Barnard, and C. Hapke (2015), Towards projecting the retreat of California's coastal cliffs during the 21st century, in *The Proceedings of the Coastal Sediments 2015 Conference*, World Sci., San Diego, Calif.

Long, J. W., and N. G. Plant (2012), Extended Kalman filter framework for forecasting shoreline evolution, *Geophys. Res. Lett.*, *39*, L13603, doi:10.1029/2012GL052180.

Luijendijk, A. P., R. Ranasinghe, M. A. de Schipper, B. A. Huisman, C. M. Swinkels, D. J. Walstra, and M. J. Stive (2017), The initial morphological response of the Sand Engine: A process-based modelling study, *Coast. Eng.*, *119*, 1–14.

Miller, J. K., and R. G. Dean (2004), A simple new shoreline change model, *Coast. Eng.*, *51*(7), 531–556.

Moin, P. (2010), *Fundamentals of Engineering Numerical Analysis*, Cambridge Univ. Press, New York.

Murray, A. B. (2007), Reducing model complexity for explanation and prediction, *Geomorphology*, *90*(3), 178–191.

National Research Council (2012), *Sea-Level Rise for the Coasts of California, Oregon, and Washington: Past, Present, and Future*, National Academies Press, Washington, D. C.

Nicholls, R. J., J. R. French, and B. van Maanen (2016), Simulating decadal coastal morphodynamics, *Geomorphology*, *256*, 1–2.

Pape, L., Y. Kuriyama, and B. G. Ruessink (2010), Models and scales for cross-shore sandbar migration, *J. Geophys. Res.*, *115*, F03043, doi:10.1029/2009JF001644.

Payo, A., J. W. Hall, J. French, J. Sutherland, B. van Maanen, R. J. Nicholls, and D. E. Reeve (2016), Causal loop analysis of coastal geomorphological systems, *Geomorphology*, *256*, 36–48.

Pelnard-Considere, R. (1956), Essai de theorie de l'evolution des formes de rivage en plages de sable et de galets, Société hydrotechnique de France.

Ranasinghe, R., and M. J. Stive (2009), Rising seas and retreating coastlines, *Clim. Change*, *97*(3), 465–468.

Ranasinghe, R., D. Callaghan, and M. J. Stive (2012), Estimating coastal recession due to sea level rise: Beyond the Bruun rule, *Clim. Change*, *110*(3-4), 561–574.

Ranasinghe, R. W. M. R. J. B., D. Callaghan, and D. Roelvink (2013), Does a more sophisticated storm erosion model improve probabilistic erosion estimates? In *Coastal Dynamics 2013*: *7th International Conference on Coastal Dynamics, Arcachon, France, 24-28 June 2013*. Bordeaux University.

Ranasinghe, R. (2016), Assessing climate change impacts on open sandy coasts: A review, *Earth Sci. Rev.*, *160*, 320–332.

Ratliff, K. M., and A. B. Murray (2014), Modes and emergent time scales of embayed beach dynamics, *Geophys. Res. Lett.*, *41*, 7270–7275, doi:10.1002/2014GL061680.

Roelvink, J. A., and G. K. F. M. Van Banning (1995), Design and development of DELFT3D and application to coastal morphodynamics, *Oceanogr. Lit. Rev.*, *11*(42), 925.

Roelvink, D., A. J. H. M. Reniers, A. Van Dongeren, J. Van Thiel de Vries, J. Lescinski, and R. McCall (2010), XBeach model description and manual. *Unesco-IHE Institute for Water Education, Deltares and Delft University of Technology. Report June*, *21*, 2010.

Rosati, J. D., R. G. Dean, and T. L. Walton (2013), The modified Bruun rule extended for landward transport, *Mar. Geol.*, *340*, 71–81.

Rueda, A., C. A. Hegermiller, J. A. A. Antolinez, P. Camus, S. Vitousek, P. Ruggiero, P. L. Barnard, L. H. Erikson, A. Tomás, and F. J. Mendez (2017), Multiscale climate emulator of multimodal wave spectra: MUSCLE-spectra, *J. Geophys. Res. Oceans*, *122*, doi:10.1002/2016JC011957.

Sallenger, A. H., Jr., K. S. Doran, and P. A. Howd (2012), Hotspot of accelerated sea-level rise on the Atlantic coast of North America, *Nat. Clim. Change*, *2*(12), 884–888.

Schwab, W. C., W. E. Baldwin, C. J. Hapke, E. E. Lentz, P. T. Gayes, J. F. Denny, J. H. List, and J. C. Warner (2013), Geologic evidence for onshore sediment transport from the inner continental shelf: Fire Island, New York, *J. Coast. Res.*, *29*(3), 526–544.

Shope, J. B., C. D. Storlazzi, L. H. Erikson, and C. A. Hegermiller (2016), Changes to extreme wave climates of islands within the Western Tropical Pacific throughout the 21st century under RCP 4.5 and RCP 8.5, with implications for island vulnerability and sustainability, *Global Planet. Change*, *141*, 25–38.

Splinter, K. D., I. L. Turner, and M. A. Davidson (2013), How much data is enough? The importance of morphological sampling interval and duration for calibration of empirical shoreline models, *Coast. Eng.*, *77*, 14–27.

Splinter, K. D., I. L. Turner, M. A. Davidson, P. Barnard, B. Castelle, and J. Oltman-Shay (2014), A generalized equilibrium model for predicting daily to interannual shoreline response, *J. Geophys. Res. Earth*, *119*, 1936–1958.

Stocker, T. (Ed.) (2014), *Climate Change 2013: The Physical Science Basis: Working Group I Contribution to the Fifth Assessment Report of the Intergovernmental Panel on Climate Change*, Cambridge University Press.

Sunamura, T. (1984), Quantitative predictions of beach-face slopes, *Geol. Soc. Am. Bull.*, *95*(2), 242–245.

Thieler, E. R., and W. W. Danforth (1994), Historical shoreline mapping (I): Improving techniques and reducing positioning errors, *J. Coast. Res.*, 549–563.

Thornton, E. B., A. Sallenger, J. C. Sesto, L. Egley, T. McGee, and R. Parsons (2006), Sand mining impacts on long-term dune erosion in southern Monterey Bay, *Mar. Geol.*, *229*(1), 45–58.

Tolman, H. L. (2009), User manual and system documentation of WAVEWATCH III TM version 3.14, *Techn. Note MMAB Contrib.*, *276*, 220.

US Army Corps of Engineers (1984), *Shore Protection Manual*, vol. 2, pp. 37–53 , Army Engineer Waterways Experiment Station, Vicksburg, Miss.

Van de Lageweg, W. I., K. R. Bryan, G. Coco, and B. G. Ruessink (2013), Observations of shoreline–sandbar coupling on an embayed beach, *Mar. Geol.*, *344*, 101–114.

Van den Berg, N., A. Falqués, and F. Ribas (2012), Modeling large scale shoreline sand waves under oblique wave incidence, *J. Geophys. Res.*, *117*, F03019, doi:10.1029/2011JF002177.

Van Dongeren, A., et al. (2009), MICORE: Dune erosion and overwash model validation with data from nine European field sites, *6th International Conference on Coastal Dynamics*, vol. 9, pp. 1–15, Tokyo, Japan.

Vitousek, S., and P. L. Barnard (2015), A nonlinear, implicit one-line model to predict long-term shoreline change, in *The Proceedings of the Coastal Sediments 2015*, World Sci., San Diego, Calif.

Warner, J. C., B. Armstrong, R. He, and J. B. Zambon (2010), Development of a coupled ocean–atmosphere–wave–sediment transport (COAWST) modeling system, *Ocean Model.*, *35*(3), 230–244.

Warren, I. R., and H. Bach (1992), MIKE 21: A modelling system for estuaries, coastal waters and seas, *Environ. Softw.*, *7*(4), 229–240.

Warrick, J. A., and L. A. Mertes (2009), Sediment yield from the tectonically active semiarid Western Transverse Ranges of California, *Geol. Soc. Am. Bull.*, *121*(7-8), 1054–1070.

Willis, C. M., and G. B. Griggs (2003), Reductions in fluvial sediment discharge by coastal dams in California and implications for beach sustainability, *J. Geol.*, *111*(2), 167–182.

Wolinsky, M. A., and A. B. Murray (2009), A unifying framework for shoreline migration: 2. Application to wave-dominated coasts, *J. Geophys. Res.*, *114*, F01009, doi:10.1029/2007JF000856.

Yates, M. L., R. T. Guza, and W. C. O'Reilly (2009), Equilibrium shoreline response: Observations and modeling, *J. Geophys. Res.*, *114*, C09014, doi:10.1029/2009JC005359.

Yates, M. L., R. T. Guza, W. C. O'Reilly, J. E. Hansen, and P. L. Barnard (2011), Equilibrium shoreline response of a high wave energy beach, *J. Geophys. Res.*, *116*, C04014, doi:10.1029/2010JC006681.

Young, A. P., P. N. Adams, W. C. O'Reilly, R. E. Flick, and T. Guza (2011), Coastal cliff ground motions from local ocean swell and infragravity waves in southern California, *J. Geophys. Res.*, *116*, C09007, doi:10.1029/2011JC007175.

Young, A. P., R. E. Flick, W. C. O'Reilly, D. B. Chadwick, W. C. Crampton, and J. J. Helly (2014), Estimating cliff retreat in southern California considering sea level rise using a sand balance approach, *Mar. Geol.*, *348*, 15–26.